ENGINYERIA ELECTRÒNICA ELÈCTRICA I AUTOMÀTICA

UNIVERSITAT ROVIRA I VIRGILI

Graduate Students Meeting on Electronics Engineering

Tarragona, July 12th, 2019

BOOK OF ABSTRACTS

IEEE

ENGINYERIA ELECTRÒNICA ELÈCTRICA I AUTOMÀTICA

UNIVERSITAT ROVIRA I VIRGILI

Graduate Students Meeting on Electronics Engineering

Tarragona July 12th, 2019

Program

Friday, July 12th:

Sala de Graus ETSE

9.30 - Opening

9.35 – Keynote: **Joan Daniel Prades** (Universitat de Barcelona)

“New miniaturization trends for power efficient gas sensors”

10.35 - Ph. D. Students Oral Presentations

- **Atieh Farokhnejad** - Study of Device Parameters Influence onPerformance of TFET–Based Circuits Using a Compact Model

- **Fabian Horst** - Closed-Form TAT Current Modeling Approach foran Implementation in Compact TFET Models

11.05 - Cofee Break and Poster Session

11.30 - Ph. D. Students Oral Presentations

- **David Garcia** - Active Battery Balancing Via A Switched DC-DC Converter. Description And Performance Analysis.

- **Jakob Leise** - Charge-Based Compact Modeling of Intrinsic Charges in Staggered OTFTs

- **Martí Boada** - NFC battery-less sensors using smartphones as a readers

12.15 – Keynote: **Adrian Ionescu** (École Polytechnique Fédérale de Lausanne)

“ Edge Artificial Intelligence Electronic Technologies for Global Challenges”

13.15 - Lunch

14.30 – Keynote: **Reza Salek** - (The International Agency for Research on Cancer (IARC), Lyon, France)

“Data sharing, data standards and data analysis in metabolomics a FAIR approach”

15.30 - Keynote: **Beatriu Prieto-Simon** (Universitat Rovira i Virgili)

“Next generation of diagnostic tools: from microneedles to nanochannel arrays”

17.00 - Closing

Invited Contributions
Keynote Speakers

Joan Daniel Prades

Universitat de Barcelona

New miniaturization trends for power efficient gas sensors

Power consumption is still an unsolved issue in solid-state semiconductor gas sensors. The most common sensor realizations rely on heat to come into operation and being those based on miniaturized actuators like micro heaters and micro hot plates the most (but not sufficiently) power efficient ones. In the last decade, further miniaturization, down to the nanoscale regime revealed as a promising strategy to reach negligible power consumption levels, but posed important fabrication and scalability challenges. As an alternative, light (which can today be generated with highly efficient devices like LEDs) can also be used to activate the response of this type of sensors. In consequence, dramatic power savings are being obtained recently with miniaturized LED-driven sensors. In this talk, we will go through all these aspects in detail, concluding a set of design criteria to implement power efficient gas sensors.

Reza Salek

The International Agency for Research on Cancer (IARC), Lyon, France

Data sharing, data standards and data analysis in metabolomics a FAIR approach

There is a growing awareness of the reproducibility challenge (or crises) in science and metabolomics. We need for metabolomics results to be FAIR: Findable, Accessible, Interoperable, and Reusable in terms of sharing data and the data analysis. Several approaches taken in recent years will be presented towards improving standards, reproducibility and reporting in metabolomics towards a more FAIR approach as well as an overview of computational infrastructure built for data analysis.

Beatriu Prieto

Universitat Rovira i Virgili

Next generation of diagnostic tools: from microneedles to nanochannel arrays

The unmet needs in point-of-care diagnostics are expected to be fulfilled with the next generation of tools based on highly versatile nanostructured electrochemical biosensing platforms. Tuning of the morphological features and electrochemical properties of the nanostructured material is key. Among the various materials available, porous silicon stands out since features major advantages for electrochemical analysis, such as high surface-to-volume ratio, unique charge transport properties, control over morphological features, and ease of surface modification and control of the electric properties. Here, it is shown a new set of porous silicon-based nanostructures that have been designed to unlock new sensing paradigms and achieve greater sensitivities and shorter analysis times, providing solutions for healthcare issues.

Students Oral Contributions Abstracts

Atieh Farokhnejad

Study of Device Parameters Influence onPerformance of TFET–Based Circuits Using a Compact Model

This paper seeks to address the effect of trap–assisted tunneling (TAT) and ambipolarity on the DC and transient behavior of tunnel-field effect transistors (TFETs) using a compact model. The robustness and flexibility of the numerical compact model make it possible to simulate the TFET not only as a single element but also in circuit level. Hence, it is used to simulate a TFET inverter and a 3–stage TFET ring– oscillator. To evaluate the impact of TAT and TFET ambipolarity, simulations are presented for different trap densities and drain doping concentrations. It is shown that the changes in flat–band voltage (Vfb) can drastically affect the performance of the TFET inverter, whereas ambipolarity and TAT nearly have no impact on the transient performance.

Fabian Horst

Closed-Form TAT Current Modeling Approach foran Implementation in Compact TFET Models

Tunnel field-effect transistors (TFETs) offer the possibility to achieve a subthreshold slope smaller than 60mV/dec and therefore are handled to be a possible candidate to supersede the conventional MOSFET technology in ultra-low power applications. The parasitic effect of trap-assisted tunneling (TAT), occurring at the channel junctions due to the high doping concentration of source and drain region, ruins the aforementioned advantage of TFETs. Since the TAT current directly influences the OFF-state current and hence the resulting slope of TFET, it is mandatory to consider TAT in compact TFET models.

Jakob Leise

Charge-Based Compact Modeling of Intrinsic Charges in Staggered OTFTs

This paper introduces a charge-based approach tomodel the total charges and the capacitances in staggered organic thin-film transistors (OTFTs). The charges are calculated by integrating over the charge density per gate area along the whole channel. The charges associated with the drain and source terminals are yielded by applying a linear charge partitioning scheme. For verification purposes TCAD simulation data and measurements are used. The compact model shows a good agreement with TCAD data and also agrees with measurement data to a certain degree. The advantage of the model is that it has one unique formulation that covers all operation regimes and it is physics-based.

Martí Boada

NFC battery-less sensors using smartphones as a readers

The availability of low-cost Near Field Communication (NFC) devices and the incorporation of NFC readers into most current mobile phones make NFC technology key to the development of battery-less IoT (Internet of Things) applications. This presentation introduces the main concerns for wireless power transfer within the NFC scenario as well as an overview of recent sensors developed including soil moisture, water content, colorimeter and body-implanted sensor.

Juan Casanova

Gas Sensors based on Diamondoid Nanostructures

Diamondoids difunctionalized with hydroxyl and primary phosphine oxide groups, enable the assembly of the first sp3-C-based chemical sensors. Both pristine nanodiamonds and palladium nanolayered composites can be used to detect toxic gases. These sensors allow a reversible NO_2 detection down to 50 ppb and NH_3 detection at 25–100 ppm concentration with fast response and recovery processes at 100^oC.

David García Elvira

Active Battery Balancing Via A Switched DC-DC Converter. Description And Performance Analysis.

This paper presents a new converter-based active balancing topology. This equalizer topology consists of a single non-isolated DC/DC converter and cell-to-cell power routing via controlled switches, which are operated as power multiplexers. The design and control strategy of the equalizer are explained. Its performance is assessed in simulation. The equalizer balances an imbalanced battery pack of five monobloc batteries, compensating the initial SOC deviations and keeping the pack balanced from then on. The influence of four battery parameters in SOC divergence is analyzed.

Students Proceedings

Closed-Form TAT Current Modeling Approach for an Implementation in Compact TFET Models

Fabian Horst[1,2,✠], Atieh Farokhnejad[1,2], Benjamín Iñíguez[2] and Alexander Kloes[1]
[1]NanoP, TH Mittelhessen University of Applied Sciences, Giessen, Germany,
[2]DEEEA, Universitat Rovira i Virgili, Tarragona, Spain,
✠fabian.horst@ei.thm.de

I. INTRODUCTION

Tunnel field-effect transistors (TFETs) offer the possibility to achieve a subthreshold slope smaller than $60\,\mathrm{mV/dec}$ and therefore are handled to be a possible candidate to supersede the conventional MOSFET technology in ultra-low power applications [1]. The parasitic effect of trap-assisted tunneling (TAT), occurring at the channel junctions (see Fig. 1) due to the high doping concentration of source and drain region, ruins the aforementioned advantage of TFETs [2]. Since the TAT current directly influences the OFF-state current and hence the resulting slope of TFET, it is mandatory to consider TAT in compact TFET models.

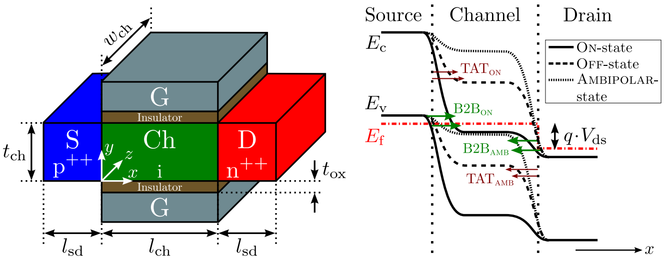

(a) (b)

Figure 1. (a) 3D device geometry of an n-type DG TFET showing its structural parameters. (b) Schematic band diagram of a Si n-type TFET for the ON-, OFF-state and the AMBIPOLAR-state of the device along the x-axis for any y-position in the channel. Green arrows: Band-to-band (B2B) tunneling. Dark red arrows: TAT.

II. COMPACT TAT MODEL

This work presents a closed-form modeling approach to characterize the TAT effect in double-gate (DG) n-type TFETs as it is shown in Fig. 1(a). The approach is based on the recombination model of *Hurkx et al.* [3] and distinguishes between TAT at the source-to-channel junction, related to the ON-state, and TAT occurring at the drain-to-channel junction which is assigned to the AMBIPOLAR-state of the TFET. The TAT current density along the y-axis is calculated by [4]:

$$J_{y,\mathrm{TAT}}^{\mathrm{s/d}}(y) = q \cdot \int\limits_{x} \frac{4\pi m_{\mathrm{s/d}}^{*}}{h^3} \cdot \tau_{\mathrm{TAT}}^{\mathrm{s/d}} \cdot N_{\mathrm{t}}^{\mathrm{s/d}} \cdot F^{\mathrm{s/d}} \cdot (1+\Gamma^{\mathrm{s/d}}) \cdot q|\vec{E}|\,\mathrm{d}x$$

$$J_{y,\mathrm{TAT}}^{\mathrm{s/d}}(y) = q \cdot \int\limits_{x} \mathrm{TGR}_{\mathrm{TAT}}^{\mathrm{s/d}}(x,y)\,\mathrm{d}x, \tag{1}$$

with the effective carrier mass $m_{\mathrm{s/d}}^{*}$, the Planck constant h, the capture cross section $\tau_{\mathrm{TAT}}^{\mathrm{s/d}}$, the trap density $N_{\mathrm{t}}^{\mathrm{s/d}}$, the supply function $F^{\mathrm{s/d}}$, the enhancement factor $\Gamma^{\mathrm{s/d}}$, the elementary charge q and the electric field $\vec{E}$. For a more detailed explanation the reader is kindly asked to refer to [5].

The TGR characterizes the TAT generation rate and is approximated by a Gaussian distribution function, which is integrable in closed-form:

$$\mathrm{TGR}_{\mathrm{c,TAT}}^{\mathrm{s/d}}(x,y) = \mathrm{TGR}_{\mathrm{max,TAT}}^{\mathrm{s/d}}(y) \cdot \exp\left(-\left(\frac{x - x_{\mathrm{max,TAT}}^{\mathrm{s/d}}}{\sigma_{\mathrm{TAT}}^{\mathrm{s/d}}}\right)^2\right), \tag{2}$$

using the maximum TGR value $\mathrm{TGR}_{\mathrm{max,TAT}}^{\mathrm{s/d}}(y) = \mathrm{TGR}_{\mathrm{TAT}}(x_{\mathrm{max,TAT}}^{\mathrm{s/d}}, y)$ at the x-position $x_{\mathrm{max,TAT}}^{\mathrm{s/d}}$, thereby $x_{\mathrm{max,TAT}}^{\mathrm{s}}$ is an adjustable parameter and $x_{\mathrm{max,TAT}}^{\mathrm{d}}$ is given by $(l_{\mathrm{ch}} - x_{\mathrm{max,TAT}}^{\mathrm{s}})$. The standard deviation of the Gaussian distribution $\sigma_{\mathrm{TAT}}^{\mathrm{s/d}}$ is used as a fitting parameter. Integrating Eq. (2) results in the current density along the y-axis:

$$\begin{aligned} J_{y,\mathrm{TAT}}^{\mathrm{s/d}}(y) &= q \cdot \int\limits_{0}^{\frac{l_{\mathrm{ch}}}{2}} \mathrm{TGR}_{\mathrm{c,TAT}}^{\mathrm{s/d}}(x,y)\,\mathrm{d}x \\ &= q \cdot \frac{\sqrt{\pi} \cdot \sigma_{\mathrm{TAT}}^{\mathrm{s/d}} \cdot \mathrm{TGR}_{\mathrm{max,TAT}}^{\mathrm{s/d}}}{2} \cdot \mathrm{erf}\left(\frac{x - x_{\mathrm{max,TAT}}^{\mathrm{s}}}{\sigma_{\mathrm{TAT}}^{\mathrm{s/d}}}\right)\Bigg|_{0}^{\frac{l_{\mathrm{ch}}}{2}}, \end{aligned} \tag{3}$$

with the error function erf. Since $x_{\mathrm{max,TAT}}^{\mathrm{d}}$ is dependent on $x_{\mathrm{max,TAT}}^{\mathrm{s}}$ and using the symmetry of the error function, the integration limits in the AMBIPOLAR-state are the same ones as in the ON-state by replacing $x_{\mathrm{max,TAT}}^{\mathrm{d}}$ by $x_{\mathrm{max,TAT}}^{\mathrm{s}}$.

Equation (3) is approximated by a Gaussian distribution by selecting two y-values to include 2D effects: $y_{\mathrm{sur}} = 0\,\mathrm{nm}$ and $y_{\mathrm{cen}} = {}^{t_{\mathrm{ch}}}/2$. The compact current density is defined by:

$$J_{\mathrm{c,TAT}}^{\mathrm{s/d}}(y) = J_{\mathrm{c,max}}^{\mathrm{s/d}} \cdot \exp\left(-\left(\frac{y - y_{\mathrm{max}}}{\eta^{\mathrm{s/d}}}\right)^2\right) + J_{y,\mathrm{TAT}}^{\mathrm{s/d}}(y_{\mathrm{cen}}), \tag{4}$$

where $\eta^{\mathrm{s/d}}$ is the standard deviation of the Gaussian distribution, used as an adjustable parameter. The maximum of the Gaussian distribution is set to $y_{\mathrm{max}} = y_{\mathrm{sur}}$ since the highest current density occurs directly under the gate oxides, thus the maximum current density is given by:

$$J_{\mathrm{c,max}}^{\mathrm{s/d}} = J_{y,\mathrm{TAT}}^{\mathrm{s/d}}(y_{\mathrm{sur}}) - J_{y,\mathrm{TAT}}^{\mathrm{s/d}}(y_{\mathrm{cen}}). \tag{5}$$

This project was supported by the German Federal Ministry of Education and Research under contract No. FKZ 13FH010IX5 and the Spanish Ministry of Economy and Competitiveness through project GREENSENSE (TEC2015-67883- R).

The device TAT current is now obtained by integrating Eq. (4) along the y-axis. By taking advantage of the DG device symmetry, which means an integration of only half of the channel thickness and a multiplication by two, the compact TAT current reads as:

$$I_{\text{ds,TAT}} = 2 \cdot w_{\text{ch}} \cdot \int_{0}^{\frac{t_{\text{ch}}}{2}} \left(J^{\text{s}}_{\text{c,TAT}}(y) + J^{\text{d}}_{\text{c,TAT}}(y) \right) \mathrm{d}y \tag{6}$$

$$= 2 \cdot w_{\text{ch}}$$

$$\times \left\{ \left[\frac{\sqrt{\pi} \cdot \eta^{\text{s}} \cdot J^{\text{s}}_{\text{c,max}}}{2} \cdot \operatorname{erf}\left(\frac{y - y_{\text{max}}}{\eta^{\text{s}}} \right) + J^{\text{s}}_{y,\text{TAT}}(y_{\text{cen}}) \cdot y \right] \Bigg|_{0}^{\frac{t_{\text{ch}}}{2}} \right.$$

$$\left. + \left[\frac{\sqrt{\pi} \cdot \eta^{\text{d}} \cdot J^{\text{d}}_{\text{c,max}}}{2} \cdot \operatorname{erf}\left(\frac{y - y_{\text{max}}}{\eta^{\text{d}}} \right) + J^{\text{d}}_{y,\text{TAT}}(y_{\text{cen}}) \cdot y \right] \Bigg|_{0}^{\frac{t_{\text{ch}}}{2}} \right\}.$$

III. MODEL VERIFICATION

The derived modeling approach is implemented in Verilog-A and extends the B2B tunneling compact model presented in [6]. The verification of the modeling approach is done by TCAD Sentaurus simulation data. 2D simulations are performed for an n-type Silicon DG TFET shown in Fig. 1(a) by applying a non-local B2B tunneling model and the model of Hurkx to consider TAT [7]. The device dimensions are as follows: $l_{\text{ch}} = 22\,\text{nm}$, $t_{\text{ch}} = 10\,\text{nm}$, $l_{\text{sd}} = 20\,\text{nm}$, $t_{\text{ox}} = 2\,\text{nm}$, $N_{\text{t}}^{0} = 10^{12}\text{cm}^{-2}$ and HfO_2 as gate oxide material.

The modeling results in terms of the current transfer characteristic for various V_{ds} are shown in Fig. 2(a). Beside the total compact modeling current compared to TCAD data, the B2B tunneling and TAT current are illustrated separately in order to demonstrate the impact of these single parts on the total current. The compact model fits very well in linear and logarithmic scale in comparison to the numerical simulation data. The influence of a change in V_{ds} on the B2B tunneling and TAT current is well predicted by the model. In the AMBIPOLAR-state the B2B tunneling and TAT current are rightwards shifted along the V_{gs}-axis for an increasing V_{ds}. The smaller V_{ds}, the sooner the B2B tunneling and TAT current in the ON-state of the TFET saturates for high V_{gs} values. This is because of the occurring inversion charges, which pin the electrostatic potential in channel to the applied V_{ds}. In Fig. 2(b) the current transfer curve for various trap densities N_{t}^{0} is illustrated. The simulation results of the compact model are compared to TCAD data. In order to capture the increasing slope of the OFF-state TAT current, the parameter $\varkappa_{\text{TAT}}{}^{\text{s/d}}$ [5] in the trap density N_{t}s/d is slightly changed. Since this parameter also influences the amount of the TAT current, the parameter $\tau_{\text{TAT}}^{\text{s/d}}$ is adapted as well. The model shows a good fit for a varying trap density by slightly adjusted model parameters. It can be seen that an increasing N_{t}^{0} has a direct influence on the resulting OFF-state TAT current and the subthreshold slope. Furthermore, the ON/OFF-ratio worsens for an increasing midgap trap density.

IV. CONCLUSION

The presented work introduced a compact modeling approach for physics-based calculation of the OFF-state or TAT current in TFETs. All modeling equations have been solved in closed-form and are suitable for an implementation in Verilog-A. The compact model has been derived for a DG TFET but is not limited to this structure. The verification was done by TCAD Sentaurus simulation data to get an insight in the device behavior. The compact model has shown a good match for the TCAD simulations. The subthreshold slope degradation was very well recognizable for high trap densities.

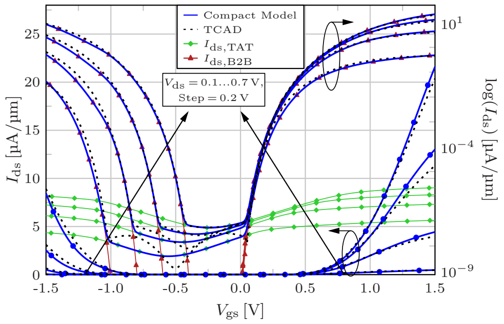

(a) Transfer curve: Various V_{ds}

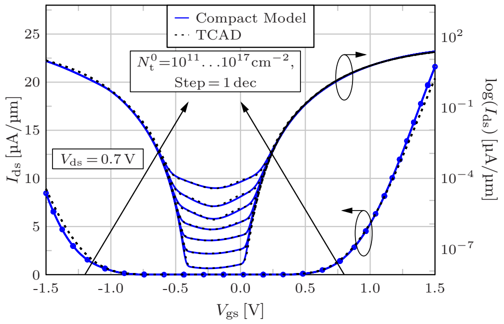

(b) Transfer curve: Various N_{t}^{0}

Figure 2. Current transfer curves of the DG n-type TFET for various (a) drain-source voltages V_{ds}, (b) trap densities N_{t}^{0}. Compact model: solid lines. TCAD: dashes lines. In (a) B2B tunneling current: red lines with triangular symbol. TAT current: green lines with diamond symbol.

REFERENCES

[1] H. Lu and A. Seabaugh, "Tunnel field-effect transistors: State-of-the-art," *IEEE Journal of the Electron Devices Society*, vol. 2, no. 4, pp. 44–49, Jul. 2014.

[2] A. Schenk, S. Sant, K. Moselund, and H. Riel, "How non-ideality effects deteriorate the performance of tunnel FETs," in *2017 IEEE Electron Devices Technology and Manufacturing Conference (EDTM)*, Feb. 2017, pp. 126–127.

[3] G. A. M. Hurkx, D. B. M. Klaassen, and M. P. G. Knuvers, "A new recombination model for device simulation including tunneling," *IEEE Transactions on Electron Devices*, vol. 39, no. 2, pp. 331–338, Feb. 1992.

[4] D. Ielmini, A. S. Spinelli, M. A. Rigamonti, and A. L. Lacaita, "Modeling of SILC based on electron and hole tunneling – part I: transient effects," *IEEE Transactions on Electron Devices*, vol. 47, no. 6, pp. 1258–1265, Jun. 2000.

[5] F. Horst, A. Farokhnejad, B. Iñíguez, and A. Kloes, "Closed-form modeling approach of trap-assisted tunneling current for use in compact TFET models," in *2019 26th International Conference "Mixed Design of Integrated Circuits and System" (MIXDES)*. IEEE, Jun. 2019, (Accepted for Publication).

[6] F. Horst, A. Farokhnejad, Q. Zhao, B. Iñíguez , and A. Kloes, "2-D physics-based compact DC modeling of double-gate tunnel-FETs," *IEEE Transactions on Electron Devices*, vol. 66, no. 1, pp. 132–138, Jan 2019.

[7] Synopsys, *TCAD Sentaurus*, Version O-2018.06 ed. Synopsys Inc., Jun. 2018.

Equivalent Length Concept for Compact Modeling of Short-Channel GAA and DG MOSFETs

Kerim Yılmaz^{1,2,*}, Ghader Darbandy^{1}, Benjamín Iñíguez^{2}, François Lime^{2} and Alexander Kloes^{1}
^{1}NanoP, TH Mittelhessen University of Applied Sciences, Giessen, Germany,
^{2}DEEEA, Universitat Rovira i Virgili, Tarragona, Spain,
*e-mail: kerim.yilmaz@ei.thm.de, phone: +49 641 309 1965

***Abstract*—We present a way to analytically describe short-channel effects in cylindrical gate-all-around (GAA) MOSFETs with intrinsic or lightly-doped channels. For a given device dimension, the center and surface potentials (Φ_C and Φ_S) are correctly determined by using the conformal mapping technique for 2-D double-gate (DG) FETs. An equivalent channel length is used in a compact drain current model of a DG device, which thereby is modified to get result for a cylindrical GAA MOSFET. To verify the introduced equivalent correlation for different channel lengths and thicknesses we compare both potentials Φ_C and Φ_S, the subthreshold swing (S_{sth}) and the drain-induced barrier lowering (DIBL) of our new compact model with 3-D GAA MOSFET TCAD simulation data. In addition, we compare for one chosen device dimension the DC characteristics of our model with TCAD and measurement data.**

***Index Terms*—Compact Model, Device Simulation, Double-Gate (DG), Nanowire GAA FET, Equivalent Dimensions, Short Channel.**

I. INTRODUCTION

For an ideal subthreshold swing and to reduce the DIBL effect in short channel devices, it is necessary to surround the complete channel with gate material. As a consequence the electrostatic control of the gate electrode in GAA MOSFETs is much better than in DG MOSFETs. By cutting a cylindrical GAA MOSFET of radius R lengthwise through the center we get a 2-D DG MOSFET of thickness $t_{ch} = 2R$ (see Fig. 1). This means, if we know the electrostatic behavior of the 2-D structure, we can trace back to the 3-D structure due to the rotational symmetry. By considering the subthreshold region the most important values, which are needed are position and value of Φ_C and Φ_S. Earlier evanescent-mode analysis [1] predict that DG MOSFETs have to be scaled to a 53 % larger channel length than GAA MOSFETs in order to provide the same immunity to short-channel effects. TCAD simulations show that a fixed conversion factor of 1.53 is not usable for all device dimensions, especially for short channel devices. In addition, Φ_C and Φ_S need different conversion factors. Therefore, we derive an analytical expression which shows a dependence on the channel thickness $t_{ch} = 2 \cdot R$ and oxide thickness t_{ox}.

II. CONVERSION FACTOR FOR THE CHANNEL LENGTH

We considered a parabolic potential Φ through the channel thickness and derived an equation for the so-called natural length λ by solving the 2-D Laplace equation along the channel/oxide interface in cylindrical coordinates:

$$\lambda^S_{GAA} = \sqrt{\frac{1}{2}\kappa\ t_{ox}R\left(\frac{R}{t_{ox}}\ln\left(1+\frac{t_{ox}}{R}\right)\right)}, \qquad (1)$$

where $\kappa = \epsilon_{ch}/\epsilon_{ox}$, ϵ_{ch} and ϵ_{ox} are the dielectric constants of Si and HfO$_2$, R is the half channel thickness and t$_{ox}$ is the gate oxide thickness. Yan et al. [2] does the same in Cartesian coordinates. Suzuki et al. [3] and Auth et al. [4] derive λ along the channel center, in Cartesian and in cylindrical coordinates, respectively. In all four cases the potential drops exponentially along the channel as $\Phi(r,z) \propto \exp(\pm z/\lambda)$. To obtain in a DG and GAA device along the surface and center of the channel the same potential profile we compare the corresponding exponents. Thus, we get the conversion factor for coordinate z, and hence the channel length:

$$z_{DG} \quad = \quad \sqrt{2}\cdot\sqrt{\frac{t_{ox}/R}{\ln\left(1+\frac{t_{ox}}{R}\right)}}\cdot z_{GAA} \qquad (2)$$

Furthermore, Oh et al. [1] hold the view that a parabolic approximation of Φ differs widely from that of the sinusoidal solution and derive a potential $\Psi^\star$ for DG and GAA MOSFETs, which satisfies the Laplace equation. By fulfilling the boundary condition at the channel/oxide interface it follows different conversion factors for surface and center, both independent from device dimensions: $z^S_{DG} \approx 1.53 \cdot z^S_{GAA}$ and $z^C_{DG} \approx \sqrt{2}\cdot z^C_{GAA}$.

In the first place we realize by comparing DG and GAA simulation data that the sinusoidal solution of the potential gives better results at the channel/oxide interface than the parabolic ansatz. On the other hand we need a device dimensions dependent conversion factor, which is achieved with the parabolic solution. As a conclusion, combining both leads to the best solution. Thus, we obtain two different conversion factors for the surface and center potential:

$$z^S_{DG} \quad = \quad 1.53\cdot\sqrt{\frac{t_{ox}/R}{\ln\left(1+\frac{t_{ox}}{R}\right)}}\cdot z^S_{GAA} \qquad (3)$$

$$z^C_{DG} \quad = \quad \sqrt{2}\cdot\sqrt{\frac{t_{ox}/R}{\ln\left(1+\frac{t_{ox}}{R}\right)}}\cdot z^C_{GAA} \qquad (4)$$

III. MODEL VERIFICATION

Applying these conversion factors to the channel length in the analytical potential model [5] of a DG transistor we obtained the results for GAA devices shown in Figs. 2. We see an excellent agreement of Φ_C, Φ_S, DIBL and S_{sth} for different channel lengths and radius's between TCAD simulation data and our new compact model.

In Fig. 3 we compare for a chosen GAA device showing short channel effects the transfer and output characteristics. We implemented the conversion factors into the DG compact model from [6] to obtain a model for a GAA device. Once again we see that it is possible to obtain a very good match between TCAD Sentaurus data and results from the compact model.

In Fig. 4 our model is compared with measurement data of a device with 24 nm gate length. We don't know how far the dopants penetrate from source and drain into the channel. Therefore, the effective channel length is a fitting parameter in our model. It has to be 12.5 nm in order to get the right swing and DIBL. This means that the dopants penetrate from both sides in average about 5.75 nm, which is reasonable. The same penetration depth is obtained by analyzing a device with a gate length of 28 nm. This is not shown in the figures.

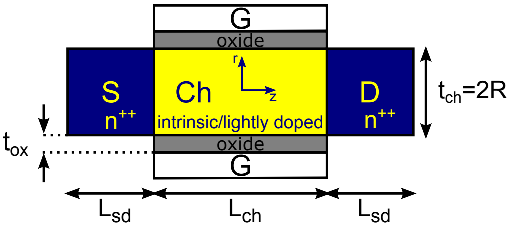

Fig. 1. Cross section of a DG/GAA MOSFET under study. S/D regions are highly n-doped and 10 nm long. The channel is intrinsic or lightly doped. The gate oxide material is HfO$_2$.

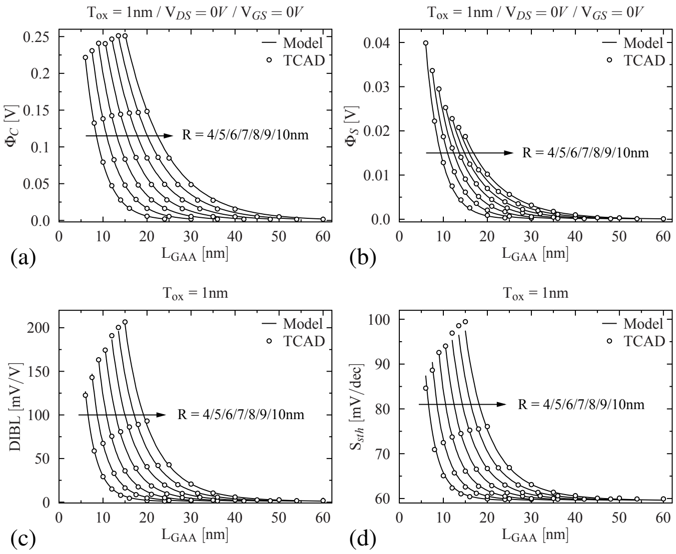

Fig. 2. Comparison of compact model (lines) with TCAD simulations (symbols) of (a) center, (b) surface potential, (c) DIBL and (d) subthreshold swing as a function of L_{GAA} with various channel radius.

IV. CONCLUSIONS

We developed an analytical concept to convert the electrostatics of a GAA to an equivalent DG MOSFET. Different scaling factors for surface and center potential relate GAA to DG concepts regarding their short-channel immunity. Thus a DG current model can be used to predict the DC behavior of ultimately scaled GAA MOSFETs.

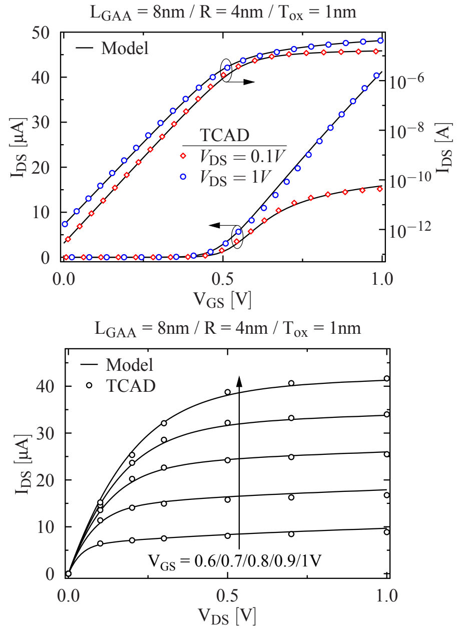

Fig. 3. Comparison of compact model with TCAD simulations of transfer and output characteristics of a short-channel GAA MOSFET.

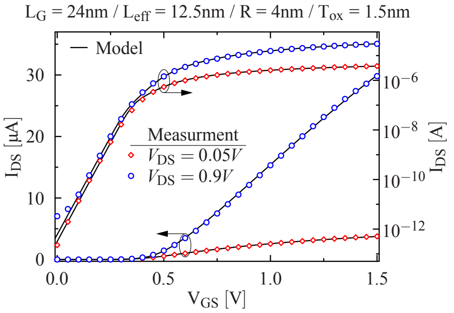

Fig. 4. Experimental data (symbols) [7] and compact model (lines) of a GAA n-MOSFET. The effective channel length L_{eff} is almost half as long as the indicated gate length L_G.

REFERENCES

[1] S.-H. Oh, D. Monroe, and J. M. Hergenrother, "Analytic description of short-channel effects in fully-depleted double-gate and cylindrical, surrounding-gate MOSFETs," *IEEE EDL*, vol. 21, no. 9, pp. 445–447, Sep. 2000.

[2] R. H. Yan, A. Ourmazd, and K. F. Lee, "Scaling the Si MOSFET: from bulk to SOI to bulk," *IEEE TED*, vol. 39, no. 7, pp. 1704–1710, Jul. 1992.

[3] K. Suzuki, T. Tanaka, Y. Tosaka, H. Horie, and Y. Arimoto, "Scaling theory for double-gate SOI MOSFET's," *IEEE TED*, vol. 40, no. 12, pp. 2326–2329, Dec. 1993.

[4] C. P. Auth and J. D. Plummer, "Scaling theory for cylindrical, fully-depleted, surrounding-gate MOSFET's," *IEEE EDL*, vol. 18, no. 2, pp. 74–76, Feb. 1997.

[5] A. Kloes, M. Schwarz, and T. Holtij, "MOS^3: A new physics-based explicit compact model for lightly doped short-channel triple-gate SOI MOSFETs," *IEEE TED*, vol. 59, no. 2, pp. 349–358, Feb. 2012.

[6] A. Kloes, M. Schwarz, T. Holtij, and A. Navas, "Quantum confinement and volume inversion in MOS^3 model for short-channel tri-gate MOSFETs," *IEEE TED*, vol. 60, no. 8, pp. 2691–2694, Aug. 2013.

[7] H. Mertens *et al.*, "Gate-all-around MOSFETs based on vertically stacked horizontal Si nanowires in a replacement metal gate process on bulk Si substrates," in *Proc. IEEE Symp. VLSI Technology*, Jun. 2016, pp. 1–2.

Charge-Based Compact Modeling of Intrinsic Charges in Staggered OTFTs

Jakob Leise, Jakob Pruefer, Ghader Darbandy, Alexander Kloes

***Abstract*—This paper introduces a charge-based approach to model the total charges and the capacitances in staggered organic thin-film transistors (OTFTs). The charges are calculated by integrating over the charge density per gate area along the whole channel. The charges associated with the drain and source terminals are yielded by applying a linear charge partitioning scheme. For verification purposes TCAD simulation data and measurements are used. The compact model shows a good agreement with TCAD data and also agrees with measurement data to a certain degree. The advantage of the model is that it has one unique formulation that covers all operation regimes and it is physics-based.**

I. INTRODUCTION

The interest in organic semiconductors (OSCs) is increasing because the fabrication process is becoming less expensive. This makes them promising candidates for large-scale, low-cost applications [1]. In OTFTs, the crystalline semiconductor is replaced by an OSC such as pentacene and the electrodes consist of a metal like gold. OSCs are characterized by their molecular orbitals. The highest occupied molecular orbital (HOMO) is the highest orbital in which an electron behaves like a bound electron and the lowest unoccupied molecular orbital (LUMO) is the lowest orbital in which an electron is in a quasi-mobile state. The energy difference between them is compared to the band gap of crystalline semiconductors. In this work, p-type OTFTs are under investigation. The amount of accumulated charge in the channel varies dependent on the bias conditions which leads to a capacitive behavior. The intrinsic charges are calculated based on the DC model presented in [2]. In order to simplify the compact model, an n-type model is considered which can be easily transferred to p-type transistors.

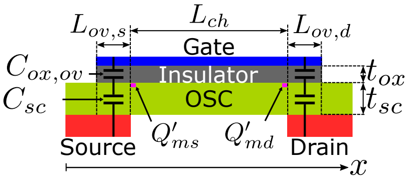

Figure 1. Structure of the staggered OTFT.

II. MODELING OF INTRINSIC CAPACITANCES

The equations for the charges are yielded assuming a quasistatic operation. This means that the charges and currents in any operation point are assumed to be the same as they would be under steady-state conditions.

A. Intrinsic Charges

The total charges associated with the channel, drain and source are yielded by integrating over the density of quasi-mobile charges per gate area along the whole channel. The charge is partitioned by applying the linear partitioning scheme according to Ward and Dutton [3]. The calculation of the total charges is based on the approach presented in [4].

$$Q_c = W_{ch} \int_0^{L_{ch}} Q'_m(x)\, dx \tag{1}$$

$$Q_d = W_{ch} \int_0^{L_{ch}} \frac{x}{L_{ch}} Q'_m(x)\, dx \tag{2}$$

$$Q_s = W_{ch} \int_0^{L_{ch}} \left(1 - \frac{x}{L_{ch}}\right) Q'_m(x)\, dx, \tag{3}$$

where x is an arbitrary position along the channel and $Q'_m(x)$ is the density of quasi-mobile charges at position x. The underlying DC model in [2] allows for the calculation of the charge densities at the source and the drain end of the channel. In order to make use of this, the integration variable has to be changed from dx to dQ'_m. Adapting the drift-diffusion model making use of the model presented in [2], dx can finally expressed as:

$$dx = -\left(\frac{W_{ch}\mu}{I_{ds}} \cdot Q'_m(x)\right) \cdot \left(\frac{\tilde{\alpha} V_{th}}{Q'_m(x)} + \frac{1}{C'_{ox}}\right) dQ'_m. \tag{4}$$

Integrating over dx from 0 to x yields an expression for the variable x. With x and dx, Eq. (1), Eq. (2) and Eq. (3) can now be solved by integrating from Q'_{ms} to Q'_{md}.

B. Overlap Charges

As it can be seen in Fig. 1, there is an overlap $L_{ov,s}$ and $L_{ov,d}$ between the gate and the source/drain electrode which is symmetric in this case and thus called L_{ov}. In staggered transistors, the overlapping electrodes are separated from each other by the gate dielectric and the OSC. This results in a series connection of two capacitances which can be calculated by the plate capacitor formula. In the off-state, the OSC behaves like an insulator with a certain dielectric constant ε_{sc}. However, in the on-state it becomes a conductor and thus, the two capacitors cannot simply be treated as a series connection over

---

This project is funded by the German Federal Ministry of Education and Research ("SOMOFLEX", No. 13FH0151IX6) and EU H2020 RISE ("DOMINO", No. 645760). We would like to thank the Max Planck Institute for Solid State Research, Stuttgart 70569, Germany for the measurement data and Keysight Technologies for the license donation of the software IC-CAP and AdMOS GmbH for support.

J. Leise, J. Pruefer, G. Darbandy and A. Kloes are with NanoP, TH Mittelhessen University of Applied Sciences, 35390 Giessen, Germany (e-mail: jakob.simon.leise@ei.thm.de).

which the voltage V_{gs} drops. In order to solve this problem, the voltage drop over the series connection is limited to

$$V_{gs}' = V_{gs} - \frac{Q_{ms}'}{C_{ox}'} \tag{5}$$

for the source side. A similar expression holds true for the drain side. In addition to the charges stored in this series connection of the capacitors, there are accumulation charges in the overlap regions. Thus, the total amount of charges accumulated in the overlap regions is the sum of the two parts mentioned above:

$$\begin{aligned} Q_{s,ov} &= \frac{C_{sc} \cdot C_{ox,ov}}{C_{sc} + C_{ox,ov}} \cdot V_{gs}' + Q_{ms}' L_{ov} W_{ch} \\ &= \frac{C_{ox,ov}}{C_{sc} + C_{ox,ov}} \cdot \left(C_{sc} V_{gs} + Q_{ms}' L_{ov} W_{ch} \right). \end{aligned} \tag{6}$$

Similar considerations hold true for the drain side which leads to the following expression:

$$Q_{d,ov} = \frac{C_{ox,ov}}{C_{sc} + C_{ox,ov}} \left(C_{sc} V_{gd} + Q_{md}' L_{ov} W_{ch} \right). \tag{7}$$

In order to account for the additional fringing charges in fabricated OTFTs, the charges are multiplied by a factor [5], [6].

C. Capacitances

The capacitances of the transistor are defined as the change of the charge at terminal i with respect to the change of the voltage at terminal j [7]:

$$C_{ij} = \begin{cases} -\frac{\delta Q_i}{\delta V_j} & i \neq j \quad i,j = g,s,d \\ \frac{\delta Q_i}{\delta V_j}, & i = j \end{cases} . \tag{8}$$

III. VERIFICATION

In this section, the compact model is verified by comparing it to the results of a Sentaurus TCAD [8] simulation and to measurements that have been conducted in [5].

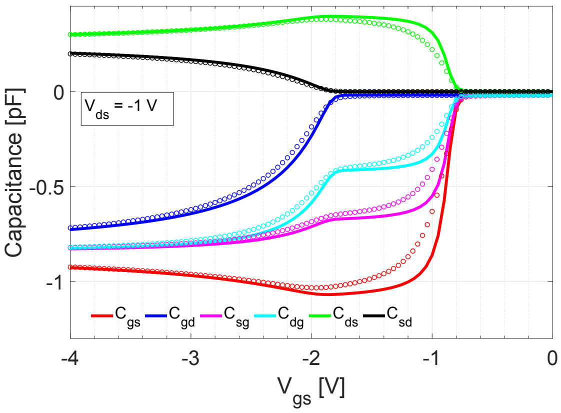

Figure 2. Capacitances of the compact model (solid lines) of a staggered device in comparison with TCAD simulation results (symbols) for $f = 0.01\,\text{Hz}$. The parameters of the transistor are: $V_{T0} = -0.86\,\text{V}$, $L_{ch} = 200\,\mu\text{m}$, $W_{ch} = 1\,\mu\text{m}$, $L_{ov,s} = L_{ov,d} = 10\,\mu\text{m}$, $S = 60\,\text{mV/dec}$. The mobility for holes in TCAD is set to $\mu_p = 1\,\text{cm}^2/\text{Vs}$ and the mobility in the compact model is set to a constant value of $\mu_p = 0.96\,\text{cm}^2/\text{Vs}$.

Fig. 3 shows the comparison of the capacitances between the compact model (solid lines) and the experimental data (symbols) [5]. There are deviations between model and experimental data which is under investigation. These deviations can be due to stress or/and hysteresis effects [9].

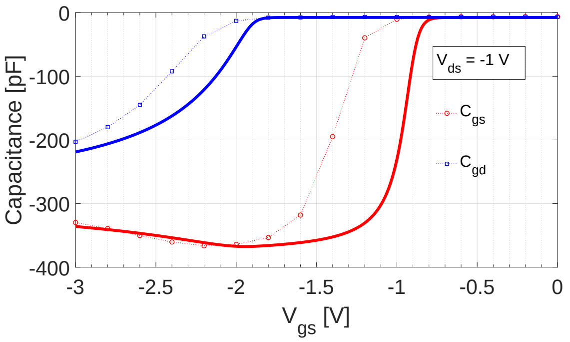

Figure 3. Capacitances of the compact model (solid lines) of a staggered device in comparison with measurement data (symbols with dotted lines) [5] for $f = 500\,\text{Hz}$. The fringing regions are accounted for by a multiplication factor of 16.5%. $L_{ch} = 200\,\mu\text{m}$, $W_{ch} = 400\,\mu\text{m}$, $L_{ov,s} = L_{ov,d} = 10\,\mu\text{m}$. The low-field mobility in the compact model is set to $\mu_{0,p} = 2.2\,\text{cm}^2/\text{Vs}$ and the empirical power-law is applied with $\beta = 0.03$. DNTT is used as OSC.

IV. CONCLUSION

This paper presented a charge-based compact model to calculate the total charges and the capacitances of OTFTs. The compact model was verified by comparing it to Sentaurus TCAD results and to measurement data. There is a good agreement between the compact model and simulation data, while there are some deviations in comparison to the measurement data. The model is being further developed in order to precisely capture the capacitive behavior of the devices.

REFERENCES

[1] L. Li, H. Marien, J. Genoe, M. Steyaert, and P. Heremans, “Compact model for organic thin-film transistor,” *IEEE Electron Device Letters*, vol. 31, pp. 210 – 212, 04 2010.

[2] F. Hain, M. Graef, B. Iñíguez, and A. Klös, “Charge based, continuous compact model for the channel current in organic thin-film transistors for all regions of operation,” *Solid-State Electronics*, vol. 133, pp. 17 – 24, 2017.

[3] D. E. Ward and R. W. Dutton, “A charge-oriented model for MOS transistor capacitances,” *IEEE Journal of Solid-State Circuits*, vol. 13, no. 5, pp. 703–708, Oct 1978.

[4] T. Holtij, “Analytical compact modeling of nanoscale multiple-gate mosfets,” Ph.D. dissertation, Department of Electronic, Electrical and Automatic Control Engineering, Universitat Rovira I Virgili, Tarragona, Spain, 2014.

[5] T. Zaki, S. Scheinert, I. Hörselmann, R. Rödel, F. Letzkus, H. Richter, U. Zschieschang, H. Klauk, and J. N. Burghartz, “Accurate capacitance modeling and characterization of organic thin-film transistors,” *IEEE Transactions on Electron Devices*, vol. 61, no. 1, pp. 98–104, Jan 2014.

[6] S. Scheinert, T. Zaki, R. Rödel, I. Hörselmann, H. Klauk, and J. N. Burghartz, “Numerical analysis of capacitance compact models for organic thin-film transistors,” *Organic Electronics*, vol. 15, no. 7, pp. 1503 – 1508, 2014.

[7] N. Arora, *MOSFET Modeling for VLSI Simulation*. World Scientific, 2007.

[8] Synopsys Inc., *TCAD Sentaurus Device User Guide*, 2012, Version G-2012.06.

[9] H. L. Gomes, *Organic field effect transistors*. Pan Stanford Publishing Pte. Ltd., March 2016.

Study of Device Parameters Influence on Performance of TFET–Based Circuits Using a Compact Model

Atieh Farokhnejad[1,2,✠], Fabian Horst[1,2], Benjamín Iñíguez[2], François Lime[2] and Alexander Kloes[1]
[1]NanoP, TH Mittelhessen University of Applied Sciences, Giessen, Germany,
[2]DEEEA, Universitat Rovira i Virgili, Tarragona, Spain,
✠atieh.farokhnejad@ei.thm.de

***Abstract*—This paper seeks to address the effect of trap–assisted tunneling (TAT) and ambipolarity on the DC and transient behavior of tunnel-field effect transistors (TFETs) using a compact model. The robustness and flexibility of the numerical compact model make it possible to simulate the TFET not only as a single element but also in circuit level. Hence, it is used to simulate a TFET inverter and a 3–stage TFET ring–oscillator. To evaluate the impact of TAT and TFET ambipolarity, simulations are presented for different trap densities and drain doping concentrations. It is shown that the changes in flat–band voltage (V_{fb}) can drastically affect the performance of the TFET inverter, whereas ambipolarity and TAT nearly have no impact on the transient performance.**

***Index Terms*—TFET inverter, ring oscillator, compact modeling, closed–form, TFET intrinsic capacitances, TAT, ambipolarity**

I. INTRODUCTION

In consideration of the fact that further scaling of integrated circuits in order to keep pace with Moore's law is reaching its physical limits, alternative structures need to be analyzed. For low–power applications, TFETs are recognized as a viable successor to the MOSFET technology due to their remarkable ability to achieve a subthreshold slope of less than 60 mV/dec [1]. Therefore, models which can characterize the TFET and also make TFET circuit level simulations possible are attracting increasing attention [2].

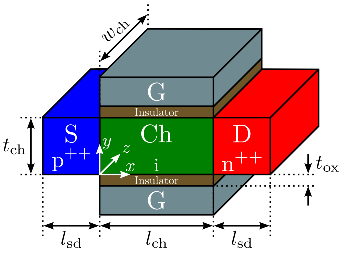

Figure 1. 3D sketch of a DG N–TFET geometry. The structural parameters are defined as: l_{ch} = 22nm, l_{sd}=20nm, t_{ch}=10nm, w_{ch} =1 μm and t_{ox}=2nm. For the source, drain and channel silicon and for the gate oxide HfO$_2$ is used.

In this work a compact DC model introduced in [3], combined with the intrinsic capacitance model in [4], is used for TFET simulations. This model is designed for Double–Gate (DG) TFET and has been shown to provide an excellent scalability with respect to physical parameters (see fig. 1). In the light of the closed–form, efficiency and predictive ability of the model, it is possible to check the influence of device parameters including trap density (N_t cm^{-2}) at the tunneling junction and drain doping concentration (N_d cm^{-3}) on TFET–based circuits without performing time consuming simulations.

II. SIMULATING SETUPS

To investigate the accuracy of our compact model, electrical characteristics of a single device are compared with those produced by TCAD Sentaurus. Afterwards, the compact model is implemented in Cadence electronic design automation software. In preliminary stages of examining the compact model, it was found that shifting V_{fb} strikingly affects the performance of the circuit. Thus, it was decided to concern two main setups for simulation; low–power (LP) and high–performance (HP) TFET. Regarding the transfer curves of the P– and N–TFET depicted in fig. 2, shifting V_{fb} by 50 mV leads to a very low I_{ds} for small supply voltages and hence, this case is called LP. In the other case V_{fb}-shift $= -200$ mV and as the result, the performance of TFET for lower V_{gs} is improved and this setup is addressed as HP. The maximum slope in the transfer characteristics of both P– and N-TFET is $\approx$ 70 in HP and $\approx$ 26 mV/dec in LP mode. This gradual slope of HP–TFETs is obviously caused by the -200 mV shift of the V_{fb}, which is used as a trade–off to reach a higher current. Based on these setups for both N– and P–TFET, an inverter is designed. Next, this circuit is used to build a ring–oscillator. For all simulations V_{DD} = 0.5 V and according to fig. 1 the channel dimensions are as following: l_{ch} = 22 nm and w_{ch} = 1 μm.

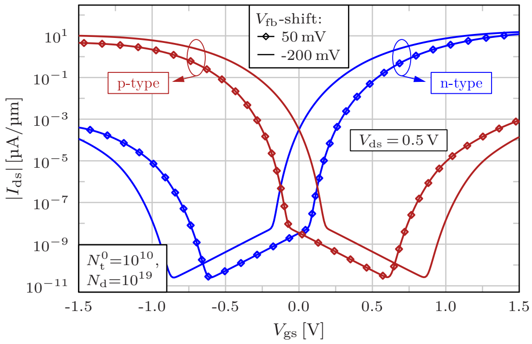

Figure 2. Transfer characteristic of DG N– and P–TFET in low (V_{fb}-shift = 50 mV) and high performance mode (V_{fb}-shift $= -200$ mV). Simulations are done at V_{ds} = 0.5 V. LP–TFETs show a higher I_{on}/I_{off} ratio for a supply voltage of 0.5 V.

III. Results and Conclutions

In fig. 3 voltage transfer curves (VTC) of the TFET inverter and also the current flow through the circuit (I_{out}), are depicted. Starting from initial state $V_{\text{in}} = 0$V, P–TFET is on and therefore $V_{\text{out}} = 0.5$V. By increasing V_{in}, N–TFET starts to conduct as well and thus, in this moment that both transistors are conducting, a path between V_{DD} and the ground is created. With further increasing V_{in} the output voltage V_{out} decreases to 0 V. In switching moment, the current flow reaches its maximum.

As it can be seen in fig. 3(a) TAT and ambipolarity do not have a compelling influence on switching performance of the HP–TFET inverter. On the other hand fig. 3(b), in which HP and LP are compared, revealed a significant difference between these two cases. The current flow through HP during switching shows a higher peak than in LP. The other point to consider is the slope of VTC curves that in LP mode is steeper as in HP which means, LP–TFETs have a higher gain. Regarding the plots, DC gain in LP is ≈ 14, whereas in HP is ≈ 3.5.

Figure 4 presents the response of the inverter to a rectangular pulse. In transient response an overshoot and undershoot in V_{out} respectively for rising and falling of the input pulse can be seen. It happens due to the intrinsic capacitances in TFET model. At $V_{\text{in}} = 0$ V, P–TFET is in the on state and holes are accumulated in its channel. While switching, the channel charges of both TFETs act as Miller capacitance. By increasing V_{in}, before the N-TFET starts to response, V_{out} is overshooting and raises up over V_{DD} [5]. Now, holes from the channel can flow through the forward-biased n-i-p junction of the P–TFET. When the N–TFET turns on, its channel is accumulated with electrons tunneling through the barrier on the source side. Hence, this charging effect slows down the deceleration of the output voltage. In HP case, the N–TFET starts to conduct earlier than in LP case, which means, the peak of overshoot is smaller. Moreover, the channel charge of the transistor, which is turn to get on, is built up faster since it is supplied by a higher current. For $V_{\text{in}} = 0.5$ V, P–TFET capacitances are discharged and N–TFET is turned on with electrons accumulated in its channel. When V_{in} begins to fall, this time N–TFET is forward-biased while V_{out} is undershooting and releasing its electrons to the ground. The tunneling current through P–TFET's source, supplies holes to its channel, limiting the drain current and consequently the rise time of the output. Figure 5 shows the output of the ring–oscillator over the time axis. Here also because of the neglectable effects of N_{t} and N_{d}, the focus is laid on HP– and LP–TFET. Considering the behavior of inverter shown in fig. 4, it could be anticipated that the ring–oscillator in HP shows a smaller delay than in LP mode and it is indeed the case.

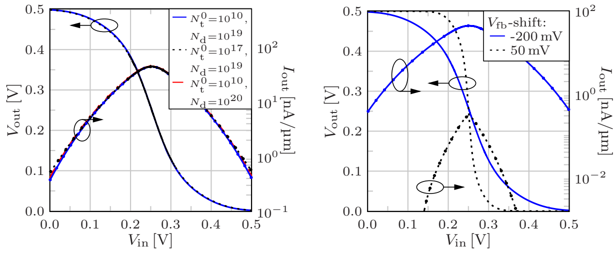

(a) (b)

Figure 3. VTC and current curve of TFET inverter. a) Several different trap densities and drain doping concentrations at V_{fb}-shift = -200 mV are employed. b) V_{fb}-shift is varied for $N_{\text{t}} = 10^{10}$ cm^{-2} and $N_{\text{d}} = 10^{19}$ cm^{-3}. For P–TFET V_{DD} = -0.5 V and for N–TFET it is set to 0.5 V.

Simulations were not time-consuming and their results fulfill the expectations. Thus, the model allows thorough static and transient analysis of digital TFET circuits, considering the influence of non–ideal effects such as TAT or ambipolar conduction on their performance.

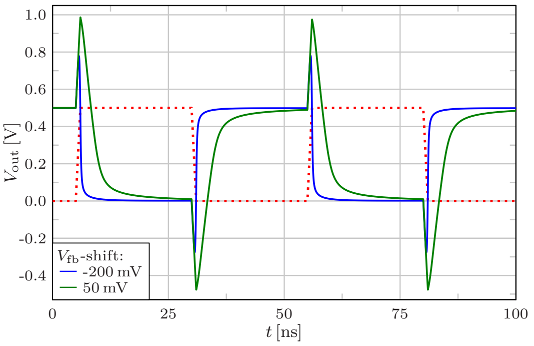

Figure 4. Impact of V_{fb}-shift on the output waveform of the TFET inverter. Input of the inverter is a rectangular pulse which is shown by red dotted line. For P–TFET V_{DD} = -0.5 V and for N–TFET it is set to 0.5 V.

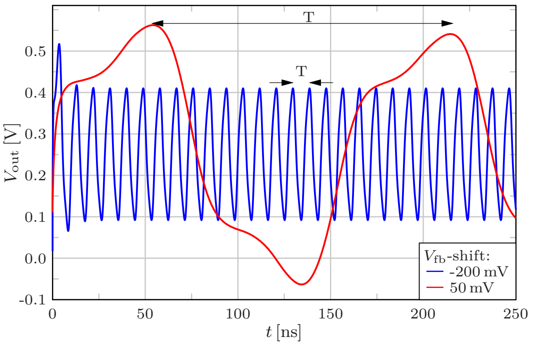

Figure 5. Output waveform of the 3–stage ring–oscillator. T presents the period of the oscillation. Depending on the V_{fb}-shift oscillation frequency of the circuit changes. For both cases the supply voltage is equal to 0.5 V.

Acknowledgment

This project was supported by the German Federal Ministry of Education and Research under contract No. FKZ 13FH010IX5 and the Spanish Ministry of Economy and Competitiveness through project GREENSENSE (TEC2015-67883- R). We would like to thank Keysight Technologies and AdMOS GmbH for their support.

References

[1] A. C. Seabaugh and Q. Zhang, "Low-voltage tunnel transistors for beyond CMOS logic," *Proceedings of the IEEE*, vol. 98, no. 12, pp. 2095–2110, Dec. 2010.

[2] E. Gnani, M. Visciarelli, A. Gnudi, S. Reggiani, and G. Baccarani, "TFET inverter static and transient performances in presence of traps and localized strain," *Solid-State Electronics*, 2019.

[3] F. Horst, A. Farokhnejad, Q.-T. Zhao, B. Iñíguez, and A. Kloes, "2-d physics-based compact DC modeling of double-gate tunnel-FETs," *IEEE Transactions on Electron Devices*, vol. 66, no. 99, pp. 1–7, 2018.

[4] A. Farokhnejad, M. Schwarz, F. Horst, B. Iñíguez, F. Lime, and A. Kloes, "Analytical modeling of capacitances in tunnel–FETs including the effect of schottky barrier contacts," *Solid-State Electronics*, 2019.

[5] C. Sahu and J. Singh, "Device and circuit performance analysis of double gate junctionless transistors at l_g = 18 nm," *The Journal of Engineering*, vol. 2014, no. 3, pp. 105–110, 2014.

Battery-less NFC sensor for PH monitoring

Martí Boada Navarro

marti.boada@urv.cat , PhD student at Department of Electronic, Electrical and Automatic Engineering, Universitat Rovira i Virgili, Tarragona, 43007, Spain.

Abstract

A low-cost battery-less colour sensor based on Near Field Communication (NFC) is presented. This system consists of a colour sensor connected to a low-power microcontroller connected to an NFC chip. The energy needed to power up the chipset is retrieved from the magnetic field generated by the reader, i.e. a commercial smartphone. The low cost of NFC chips affords the opportunity to manufacture low-cost tags with sensing capability. We have developed a mobile application to simultaneously present the data and send them to a database in the cloud. The system has been tested with several pH reactive strips. pH was determined via colour measurement using the HSV colour space. A simple linear relationship was found between the Hue parameter and the pH. Comparison with pH determination via smartphone camera showed that accuracy was greater when the NFC colorimeter was used.

1. Introduction

Microfluidic paper-based devices for analyses based on colour determination are widespread in applications such as medical devices [1] and pH measurements [2]. The main advantages of these devices are that they are inexpensive, do not require an energy source, allow for easy transportation of fluids, and are easy to use. However, since diagnosis depends on optical measurements, accuracy is poor especially when, as in pH measurements, classification between different levels is required. PH measurement has a wide range of applications.

In this work we present a low-cost NFC-based system that combines an NFC IC for communications and a colorimeter IC with a microcontroller. The tag is completely passive and takes energy from the RF interrogating signal from the reader using the energy-harvesting capabilities of the NFC IC. A simple calibration method is used to convert the measured colour of the pH strips into pH levels. We have developed a custom readout application that uses a smartphone with NFC compatibilities as a reader.

Compared to other mobile-equipped wireless standards such as Bluetooth or Wi-Fi, NFC technology presents several advantages in short-range communications. NFC ICs are cheaper, and have capability to store data within the NFC IC, avoiding the use of microcontrollers or external memories, thus reducing price, complexity, size and power consumption. They also grant the possibility of developing low-cost sensors for a wide variety of applications.

2. System Description

An overview of the system is shown in Fig. 1. This consists of an electronic circuit made up of a colour light-to-digital TCS3472 converter from TAOS [3], a white 4150 ºK LED to illuminate the sample, a low-power Atmel Tiny 85 microcontroller, and an NFC chip from ST Microelectronics (M24LR04E).

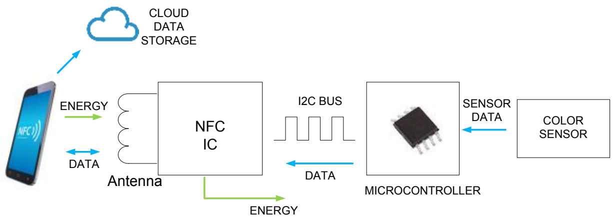

Fig.1. Block diagram of the proposed NFC-based pH sensor.

A photograph of the prototype is shown in Fig. 2. The loop antenna, the NFC IC and the microcontroller are located on the top, while the color sensor and the LED are connected on the bottom. The connector that links the two circuit boards is also used to download the firmware in the microcontroller. A plastic enclosure for the PCB was designed using a 3D printer (see Fig. 2c).

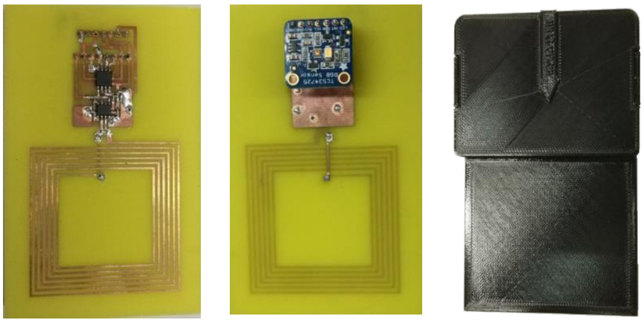
(a) (b) (c)

Fig.2. Photograph of the prototype from (a) the top and (b) the bottom and (c) the 3D printed enclosure.

3. Antenna Design and Energy Harvesting From the Smartphone

Wireless power transfer (WPT) between two coils has been widely studied [4]. NFC systems use the energy obtained from the coupling between two coils to feed the internal circuitry while performing the reading and writing operation through RF communications. In addition, NFC IC with energy harvesting capability includes a rectified voltage output to power up external circuits. Fig. 3 shows a model of the wireless power transfer between the reader and the tag.

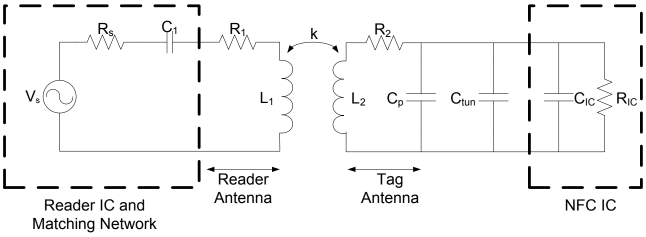

Fig.3. Wireless power transfer model between the reader and the tag.

In order to validate the performance of the system as a function of distance, several simulations using the model of Fig. 3 are done. Hence it is needed to know the main features of the antennas such as their coupling coefficient, k. The coupling coefficient of a pair of coils is a measure of the magnetic effect passing between them and therefore it is a fundamental parameter in NFC. It depends on the shape of the antennas, distance and alignment between antennas, and the materials. The coupling coefficient can be calculated from the Z parameters from electromagnetic simulations or S parameters measurements performed with VNA:

$$k = \frac{|Im(Z_{12})|}{\sqrt{Im(Z_{11}) \cdot Im(Z_{22})}} \quad (1)$$

Since each manufacturer uses different techniques to design the NFC antenna on the smartphone, three different antennas has been studied. The setup shown in Fig. 4 was used to measure the magnetic field.

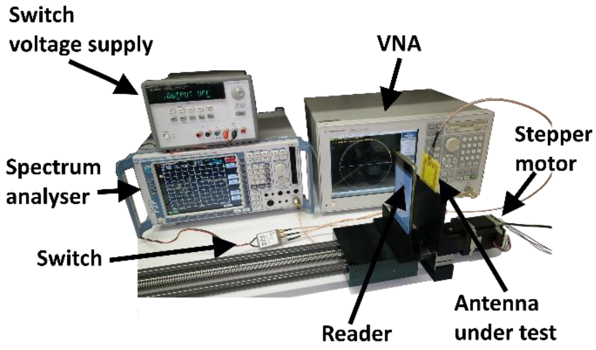

Fig.4. Setup to measure the magnetic field, composed by reader, antenna under test, spectrum analyser, VNA, SPDT switch and voltage supply.

Fig. 5 shows the Hav as a function of the distance for two mobiles. For the current consumption of the tag, a read range of between 1 cm and 2 cm is obtained, depending on which smartphone is used as a reader. This distance corresponds to a measured minimum magnetic field equal to 1.1 ARMS/m.

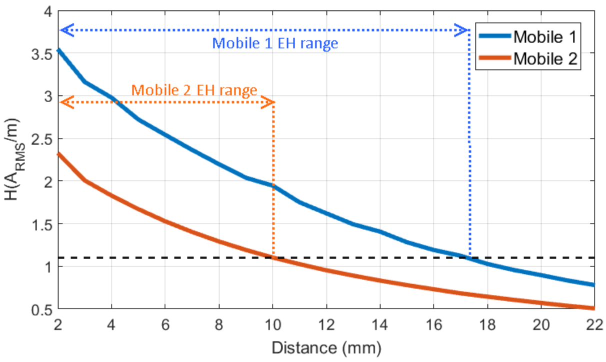

Fig.5. Setup to measure the magnetic field, composed by reader, antenna under test, spectrum analyser, VNA, SPDT switch and voltage supply

4. Signal Processing

A mathematical model is needed to transform the raw colour measurement in RGB provided by the colour sensor into pH. However, a colour model must be defined in order to digitalize a colour for its representation or analysis. One way to obtain the pH from the raw RGB measurement is to use a table-based method and an interpolation function. However, a simple model using HSV (Hue-Saturation-Value) colour space is also available and found on the literature [5][6]. This model is useful not only because it is more intuitive than raw RGB values but also because the conversions to and from RGB are extremely quick to compute and can be run in real time on the microcontroller. When shifts in colours have to be measured, the HSV (Hue Saturation Value) model should be considered. HSV is an alternative representation of RGB based on how the human eye works. Instead of measuring the portion of each primary colour, the results are expressed in terms of Hue (representing pure colour and expressed in degrees from 0º to 360º) (see Fig. 6), Saturation (percentage of white colour), and Value (brightness, expressed in percentage).

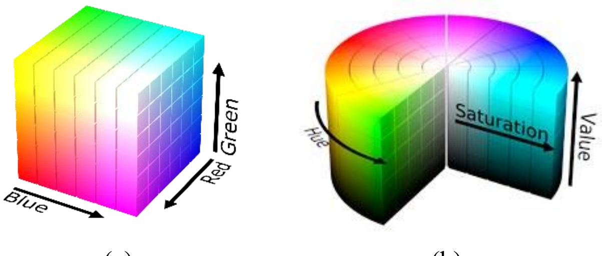

(a) (b)

Fig.6. (a) RGB colour space, (b) HSV colour space.

Fig. 7 shows that the Hue of the strips behaves in a linear fashion, thus enabling the creation of a linear regression model (the red line in Fig. 17) to characterize each type of strip. Based on this linear model, the system can be calibrated by measuring two different pH values.

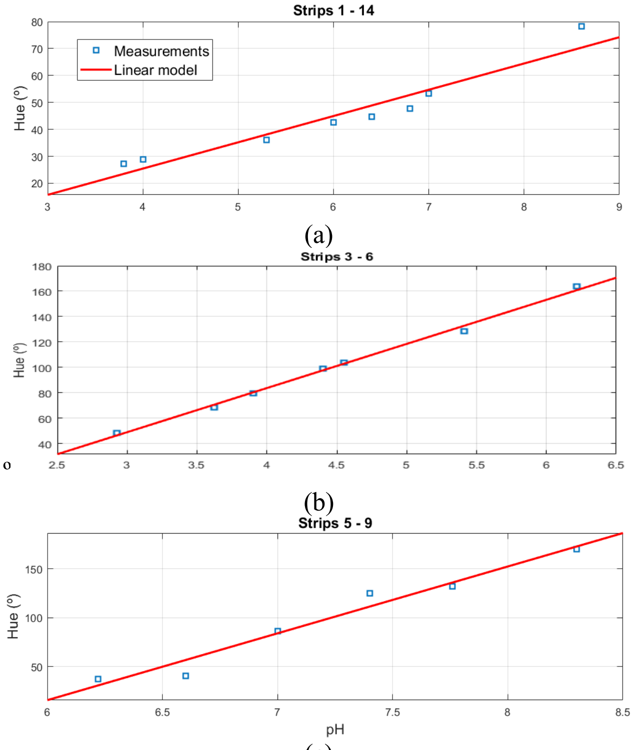

(a)

(b)

(c)

Fig.6. (a) RGB Hue measurements of several known pH values. (a) Strips 1 to 14, (b) strips 3 to 6: and (c) strips 5 to 9.

7. Conclusions

We have presented a batteryless, low-cost colorimeter integrated into an NFC tag. While this device has several applications, in this paper we apply it to the measurement of pH using pH-sensitive paper strips. Raw RGB measurements of the colorimeter IC are transformed into HSV colour space. A simple linear relationship is found between pH and Hue for typical commercial strips. The pH is obtained from this line and can be easily calibrated using a known pH solution. We found that the repeatability of the measurement is higher than for methods based on smartphone cameras because the measurements are taken in controlled light conditions. We have designed a smartphone application to read the data from the NFC tag and send the pH to a cloud database. The theoretical and experimental read range obtained for the tag prototype is up to 18 mm depending on the smartphone used. This study shows that green sensors based on NFC IC with energy harvesting capabilities can help to design a new generation of low-cost smart devices and simplify the man-machine interface. Furthermore, new NFC chips are arriving to the market with better energy harvesting capabilities supplying more energy to the tag thus increasing NFC possibilities. This opens the door to cooperative IoT for smart cities and Industry 4.0 applications.

References

[1] V. Oncescu, D. O'Dell, and D. Erickson, 'Smartphone based health accessory for colorimetric detection of biomarkers in sweat and saliva', *Lab Chip*, vol. 13, no. 16, pp. 3232–3238, 2013.

[2] S. D. Kim, Y. Koo, and Y. Yun, 'A smartphone-based automatic measurement method for colorimetric pH detection using a color adaptation algorithm', *Sensors (Switzerland)*, vol. 17, no. 7, 2017.

[3] 'TCS3472 COLOR LIGHT-TO-DIGITAL CONVERTER with IR FILTER', 2012. https://cdn-shop.adafruit.com/datasheets/TCS34725.pdf (accessed on June, 26, 2019).

[4] A. Costanzo, M. Dionigi, F. Mastri, M. Mongiardo, J. A. Russer, and P. Russer, 'Rigorous network modeling of magnetic-resonant wireless power transfer', *Wirel. Power Transf.*, vol. 1, no. 1, pp. 27–34, 2014.

[5] N. Lopez-Ruiz, V. F. Curto, M. M. Erenas, F. Benito-Lopez, D. Diamond, A. J. Palma, and L. F. Capitan-Vallvey, 'Smartphone-based simultaneous pH and nitrite colorimetric determination for paper microfluidic devices', *Anal. Chem.*, vol. 86, no. 19, pp. 9554–9562, 2014.

[6] S. Capel-Cuevas, N. López-Ruiz, A. Martinez-Olmos, M. P. Cuéllar, M. del Carmen Pegalajar, A. J. Palma, I. de Orbe-Payá, and L. F. Capitán-Vallvey, 'A compact optical instrument with artificial neural network for pH determination', *Sensors (Switzerland)*, vol. 12, no. 5, pp. 6746–6763, 2012.

Removal of Thick Barrier Layer in Nanoporous Anodic Alumina by Electrochemical Method

M.P Montero-Rama, A. Viterisi, C. Eckstein, J. Ferré-Borrull and L. F Marsal*

Nano-electronic and Photonic Systems group, Universitat Rovira i Virgili,
Avinguda dels Països Catalans, 26, 43007, Tarragona, Spain.
lluis.marsal@urv.cat.

Abstract

An innovate process for removing the thick barrier layer of nanoporous anodic alumina (NAA) based on a constant current re-anodization step is reported. Some procedures have been reported for removing the alumina layer without detaching the porous nanostructure from the aluminium substrate. Nevertheless, none of them is valid to NAA obtained under a high voltage anodization, for example with phosphoric acid (H_3PO_4) electrolyte. With this procedure, we obtain a self-ordered NAA substrates without barrier layer, letting for the establishment of an electrical contact between the aluminium substrate on which the nanopores were grown-up and the interior of the nanopores.

1. Introduction

Nanoporous anodic alumina (NAA) has attracted a great deal of interest in the last decades because of its wide range of applications.[1] The main properties of NAA are its chemical stability, its mechanical durability, the cost-effective scalable production and the ability to fabricate pores with a wide range of thicknesses, diameters and interpore distances.[2] As the NAA is obtained by anodization of aluminium foils, we can use the aluminium foil as an electrical back contact.[3] However, since the NAA presents a thick barrier layer at the bottom side, we need to remove it to obtain a good electrical contact, since this barrier layer is an insulation material.

2. Experimental and Results

NAA samples were prepared following the two-step anodization process (Fig. 1a)).[4] Followed a partially etching in H_3PO_4 was carried out (Fig. 1b)) and a re-anodized step was performed at constant density current.[5] This results in the formation of several branchings in the barrier layer (Fig. 1c)), which lead to its complete removal upon a final chemical etching step (Fig. 1d)), living at least intact the pore structure and obtaining an electrical back contact.

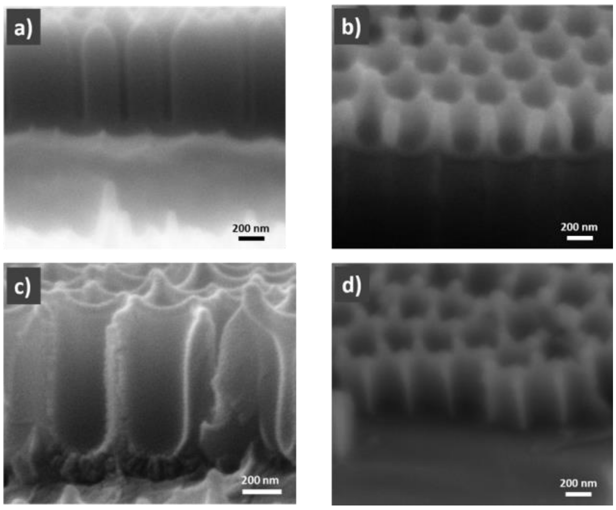

Fig.1. Cross-section ESEM views of a phosphoric NAA **a)** after the two-step anodization. **b)** after the partial chemical etching. **c)** after re-anodization step at constant density current. **d)** after final chemical etching.

In order to determine the optimal conditions for the current re-anodization step, several experiments were conducted for different values of the density current. In the Fig. 2 are plot the measured voltage *vs* time at different constant current. Since the thickness of the barrier layer increase with the voltage,[6] the experiments which the measured voltage increase, as we can see in the Fig. 2 a), b) and c) were stopped. The experiment which the measured voltage keep constant were stopped too (Fig. 2d)). We let that the experiment which the measured voltage decrease finish (Fig. 2e). The Fig. 2f) shows the branchings, but had grown through the barrier layer in a non-homogenous way.

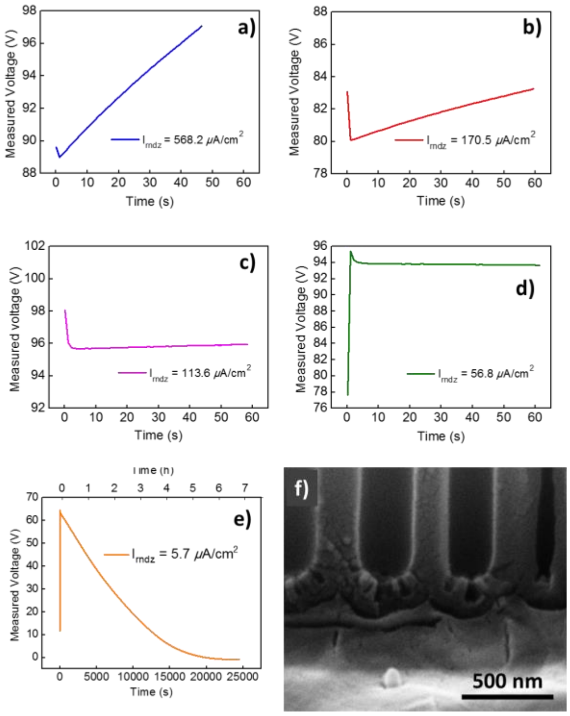

Fig. 2. (a) to **(e)**, Measured voltage vs time corresponding to each experiment. The current density for each experiment is indicated in the fig. **(f)** Cross-section ESEM view of the NAA for I_{rndz} = 5.7 μA/cm^2. The scale bar is indicated in the picture.

To obtain homogenous pores we tested a new value of density current. Fig. 3a) shows the measured voltage *vs* time at a constant current density of 17.0 μA/cm^2. Fig. 3 b) and c) shows the cross-section view of the pores, we can see a homogenous branchings in the barrier layer.

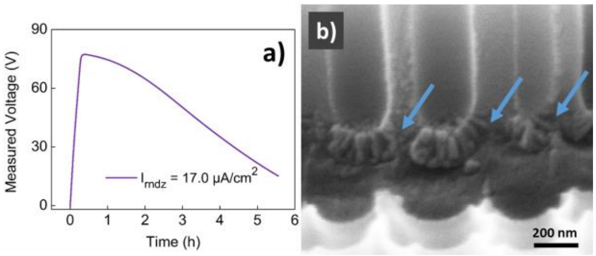

Fig. 3. (a) Measured voltage vs time for I_{rndz} = 17.0 μA/cm^2. **(b)** Cross section ESEM picture of NAA for this value of current density with the point of contact between the oxide and the aluminium marked by the arrow. The scale bar is indicated in the picture.

This barrier layer with the branchings can easily be removed with a final chemical etching step while leaving the pore walls almost intact.

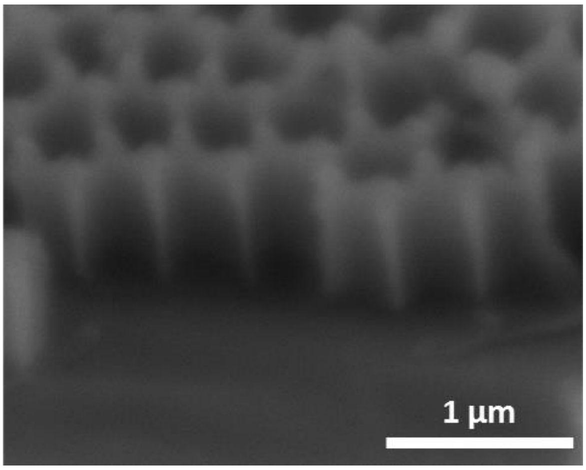

Fig. 4. Cross-section ESEM views of NAA with the barrier layer totally remove.

3. Conclusions

We present a new method for the removal of the thick barrier layer (>200 nm) in a NAA sample without removing the aluminium substrate. The re-anodization step carried out at 17.0 μA/cm^2 (Fig. 3a)) permits the creation of homogeneous branchings within the barrier layer. A final chemical etching dissolves the barrier layer with the branchings. We can infiltrate different materials into the nanopores and establish of an electric contact between the material infiltrated and the aluminium substrate.

Acknowledgements

This work was partially supported by the Spanish Ministerio de Ciencia, Innovación y Universidades (MICINN/FEDER) RTI2018-094040-B-I00, by the Agency for Management of University and Research Grants (AGAUR) ref. 2017-SGR-1527 and by the Catalan Institution for Research and Advanced Studies (ICREA) under the ICREA Academia Award.

References

[1] J. Ferré-Borrull, E. Xifre-Perez, J. Pallarès, and L. F. Marsal, “Nanoporous Alumina,” vol. 219, pp. 185–217, 2015.

[2] W. Lee and S.-J. Park, “Porous Anodic Aluminum Oxide: Anodization and Templated Synthesis of Functional Nanostructures,” *Chem. Rev.*, vol. 114, no. 15, pp. 7487–7556, Aug. 2014.

[3] A. Santos, L. Vojkuvka, J. Pallarés, J. Ferré-Borrull, and L. F. Marsal, “In situ electrochemical dissolution of the oxide barrier layer of porous anodic alumina fabricated by hard anodization,” *J. Electroanal. Chem.*, vol. 632, pp. 139–142, 2009.

[4] H. Masuda and K. Fukuda, “Ordered metal nanohole arrays made by a two-step replication of honeycomb structure of anodic alumina,” *Science,* vol. 268, no. 5216, pp. 1466–1468, June 1995.

[5] K. Nielsch, F. Müller, A.-P. Li, and U. Gösele, “Uniform Nickel Deposition into Ordered Alumina Pores by Pulsed Electrodeposition,” *Adv. Mater.*, vol. 12, no. 8, pp. 582–586, 2000.

[6] M. M. Rahman, E. Garcia-Caurel, A. Santos, L. F. Marsal, J. Pallarès, and J. Ferré-Borrull, “Effect of the anodization voltage on the pore-widening rate of nanoporous anodic alumina,” *Nanoscale Res. Lett.*, vol. 7, pp. 1–7, 2012.

Effect of thermal annealing on the performance of non-fullerene acceptor-based inverted organic solar cells

Alfonsina A. A. Torimtubun, José G. Sánchez, Josep Pallarès Marzal*, Lluis F. Marsal*

Department of Electrical Electronic Engineering and Automation, Universitat Rovira I Virgili, 43007 Tarragona, Spain
*E-mail: josep.pallares@urv.cat and lluis.marsal@urv.cat

Abstract

The effects of thermal annealing on the photovoltaic properties of inverted organic solar cells based on blends of polymer donor PBDB-T and non-fullerene small molecule acceptor ITIC-M in the device structure of ITO/TiO_2/PBDB-T:ITIC-M/V_2O_5/Ag are investigated. We found that the power conversion efficiency increases up to 66% higher as the annealing temperature is varied from room temperature to 160ºC. The open circuit voltage, short circuit current, fill factor and light absorption are sequentially enhanced and trap-assisted/bimolecular recombination are suppressed after the annealing process. These results indicate that thermal annealing treatment can significantly improve organic solar cells performance.

1. Introduction

Organic solar cells (OSCs), a photoactive blend film of binary system comprising one electron-donating and one electron-accepting semiconductor, have attracted much attention due to their low-cost, light weight, solution processability and flexible device potential application[1]. The power conversion efficiencies (PCEs) have been boosted over 14% by incorporating several approaches such as material design, device engineering, and theoretical studies[2]. Among these record efficiencies, non-fullerene acceptors (NFAs) materials afford superior PCEs which is more compatible for industrial production requirements than conventional OSCs based on fullerene acceptors (FAs). Besides their potential for low-cost production process, NFAs have shown faster development than FAs because NFAs possess readily tunable molecular structures. As a result, their optical absorption spectra, their energy levels, solubilities and crystallinities can be finely modulated to well match those of various donors[3].

Besides the active materials, device structures plays an important role in a performance of OSCs. Conventional OSCs generally have a structure in which poly(3,4-ethylenedioxythiophene):poly(styrene sulfonic acid) (PEDOT:PSS) as a hole-transporting layer (HTL) is coated on an indium-doped tin oxide (ITO). These normal OSCs has low environmental stability because the oxidation of low-work function cathode (Al) and the degradation of ITO by the acidic PEDOT:PSS. In this work, we inverted the charge collection direction to enhance the OSCs′ stability. We used titanium dioxide (TiO_2) as an electron-transporting layer (ETL) deposited on ITO because it presents good transparency as thin films, high stability and an ability to improve the charge carrier extraction[4].

Performance of the OSCs depends on the preparation conditions such as annealing treatment. After annealing, the morphology of the active layer may change under different annealing time or temperatures due to the presence of recombination mechanisms in different structures, hence affecting the performance of a solar cell. In this study, we have studied the effect of annealing temperatures and annealing times on the device performance of PBDB-T:ITIC-M based OSCs.

2. Experimental Methods

Materials. ITO patterned on glass with the resistivity of 10 Ω sq^{-1} was used as a transparent contact. Silver (Ag) was used as a back contact (counter electrode). The donor active layer materials used in this work are based on conjugated polymer PBDB-T and the non-fullerene acceptor ITIC-M. Titanium oxide (TiO_x) and vanadium oxide (V_2O_5) were used as transport layers.

Device Fabrication. The device architecture was ITO/TiO_2/PBDB-T:ITIC-M/V_2O_5/Ag. The TiO_2 layer was spin-coated on the top of a pre-cleaned, UV-ozone-treated ITO substrate. Subsequently, the active layer solution, made by dissolving PBDB-T:ITIC-M (1:1 w/w) in chlorobenzene:DIO (99.5:0.5% v/v) in 20 mg mL^{-1}, was spin-coated at 1600 rpm for 1 min. V_2O_5 (5 nm) and Ag (100 nm) were used as hole transport layer and top electrodes, deposited through shadow mask under high vacuum conditions ($\leq 1 \times 10^{-6}$ mbar). The effective area for all devices was 0.09 cm^2.

Device Characterization. The electrical properties of OSCs devices (*J-V* measurements) were obtained using a solar simulator (Abet Technologies model 11000 class type A, Xenon arc) and a Keithley 2400 Source-Measure Unit under dark and illumination conditions. The light intensity was calibrated by a NREL certified monocrystalline silicon photodiode. The ratio of the number incident photons to the number of charge carries extracted by solar cells known as external quantum efficiency (EQE) is measured by EQE measurement using homemade set up, consisting of 150 W Oriel Xenon lamp, a motorized monochromator, a Keithley 2400 digital source meter and Labview© software. The EQE measurements were carried out under forward wavelength sweep direction from 300 nm to 800 nm.

3. Results and Discussion

To investigate how thermal annealing affects the performance of OSCs, we fabricated OSCs with an inverted device structure of ITO/TiO_2/PBDB-T:ITIC-M/V_2O_5/Ag (Fig. 1a). The chemical structures of PBDB-T and ITIC-M are shown in Fig.1b. Fig.2 shows the current density–voltage (*J-V*) characteristics with the varied annealing temperature from room temperature up to 160ºC, and their photovoltaic performance parameters were summarized in Table 1. The devices based on PBDB-T:ITIC-M without thermal annealing showed a maximum PCE of 5.99% with a J_{sc} of 13.6 mA cm^{-2}, a V_{oc} of 0.84 V and an FF of 53%. By increasing the temperature at 100ºC, PCE was improved to 8.94% with higher J_{sc} of 15.8 mA cm^{-2}, a V_{oc} of 0.89 V and an FF of 64%. The OSCs device annealed at 100ºC exhibited the best photovoltaic performance. Further increasing the annealing temperature, at 160ºC, PCE was slightly decreased to 8.31% with lower J_{sc} of 15.7 mA cm^{-2}, a V_{oc} of 0.86 V and an FF of 62%.

Annealing condition	V_{OC} [V]	J_{SC} [mA cm^{-2}]	FF [%]	PCE [%]	R_s [Ω/cm^2]	R_{sh} [Ω/cm^2]
Without	0.84	13.6	0.53	5.99	7.14	478
100ºC	0.89	15.8	0.64	8.94	4.38	904
160ºC	0.86	15.7	0.62	8.31	4.36	831

Table1. Photovoltaic parameters of PBDB-T:ITIC-M–based solar cells.

The EQE spectra of OSCs were shown in Fig.3. Compared with the devices without annealing, the EQE values were enhanced in a wide wavelength ranges from 375 nm to 725 nm for the devices annealed at 100º and 160ºC, suggesting that thermal annealing treatment can enhance photon absorption.

4. Conclusions

Devices based on PBDB-T:ITIC-M after annealing at varied temperature have been thoroughly investigated. The best PCE of 8.94% was achieved with 100ºC annealing which is higher 66% compared with those without thermal annealing treatment. The V_{OC}, J_{SC}, FF and light absorption were sequentially enhanced and trap-assisted/bimolecular recombination were suppressed after the annealing process. These results indicated that thermal annealing treatment can significantly improve device performance of organic solar cells based on PBDB-T:ITIC-M.

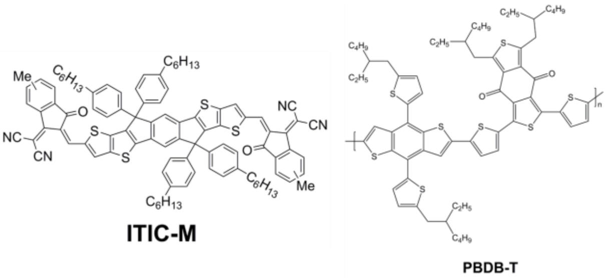

Fig.1. Chemical structures of polymer donor PBDB-T and small-molecules acceptor ITIC-M.

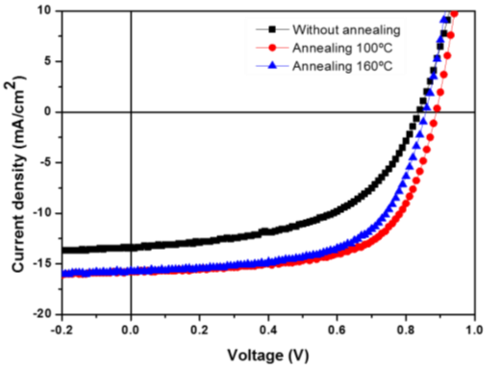

Fig.2. Current density versus voltage (*J-V*) curve

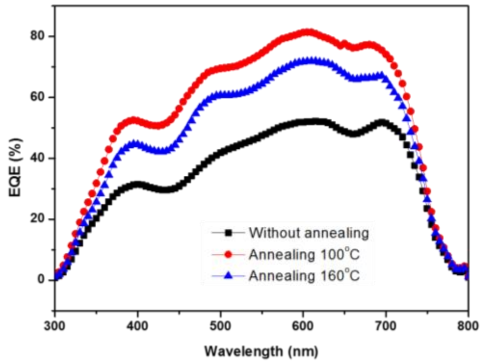

Fig.3. EQE curves of the PBDB-T:ITIC-M-based OSCs

References

[1] B. Zhao *et al.*, "Flexible polymer solar cells with power conversion efficiency of 8.7%," *J. Mater. Chem. C*, vol. 2, no. 26, pp. 5077–5082, 2014.

[2] S. Zhang, Y. Qin, J. Zhu, and J. Hou, "Over 14% Efficiency in Polymer Solar Cells Enabled by a Chlorinated Polymer Donor," *Adv. Mater.*, vol. 30, no. 20, pp. 1–7, 2018.

[3] X. Liu, Y. Yan, Y. Yao, and Z. Liang, "Ternary Blend Strategy for Achieving High-Efficiency Organic Solar Cells with Nonfullerene Acceptors Involved," *Adv. Funct. Mater.*, vol. 28, no. 29, pp. 1–20, 2018.

[4] J. G. Sánchez *et al.*, "Stability study of high efficiency polymer solar cells using TiOx as electron transport layer," *Sol. Energy*, vol. 150, pp. 147–155, 2017.

Gas Sensors based on Diamondoid Nanostructures

Juan Casanova-Chafer[1], Oana Moncea[2,3], Didier Poinsot[2], Eduard Llobet[1], Peter R. Schreiner[3], and Jean-Cyrille Hierso[2]

[1] MINOS-EMaS, University Rovira i Virgili (Spain)
[2] ICMUB, Université de Bourgogne Franche-Comté (France)
[3] Institute of Organic Chemistry, Justus Liebig University (Germany)

Abstract

Diamondoids, sp^3-hybridized nanometer-sized diamond-like hydrocarbons (nanodiamonds), difunctionalized with hydroxyl and primary phosphine oxide groups, enable the assembly of the first sp^3-C-based chemical sensors by vapor deposition. Both pristine nanodiamonds and palladium nanolayered composites can be used to detect toxic NO_2 and NH_3 gases. Semiconducting p-type sensing properties are achieved from devices based on primary phosphine–diamantanol, in which high specific area (ca. 140 m^2/g) and channel nanoporosity derive from H-bonding. This carbon-based gas sensor technology allows reversible NO_2 detection down to 50 ppb and NH_3 detection at 25–100 ppm concentration with fast response and recovery processes at 100ºC. Reversible gas adsorption and detection is also compatible with humidity conditions [1].

1. Introduction

Air pollution is associated with global climate change, causing several million deaths per year. [2] Many toxic gases are produced through combustion processes from vehicles as well as industrial plants. Nitrogen dioxide (NO_2) is the most hazardous gas with a 3 ppm threshold limit value (TLV, human level of exposure to be strictly controlled) [3]. NO_2 plays a role in atmospheric reactions causing acid rain, and contributes to ozone formation, which is the major cause of photochemical produced smog [2, 3]. Detection and emission control of nitrogen oxides are thus essential objectives to reduce their hazardous effects on environment and mankind.

Metal oxide semiconductors are low-cost, robust sensors most frequently used for the NO_2 detection [4]. These usually operate at temperatures of a few hundred degrees Celsius, which is costly and reduces sensor lifetime. Other significant limitations are cross-sensitivities with other gases, and detrimental interference from relative humidity. Thus, sensor development experienced a remarkable rise in attention focusing on sp^2-hybridized carbon structures [5]. There is, however, a large group of sp^3-hydridized carbon semiconductor materials, the so-called diamondoids, which essentially are hydrogen-terminated diamond. These structures are mechanically rigid and thermodynamically extremely stable. NO_2 adsorption is more favorable on carbon nanostructures with high metallic character, thus we envisioned that nanocomposites combining sp^3-carbon 3-D molecular-size diamondoids coated with thin metal nanolayers would yield hybrid materials with electronically modified surfaces.

2. Experimental

From diamantine powder, the primary phosphine 9-(hydroxydiamant-4-yl) phosphine (H2P–DiamOH, **1**) and its oxide ($H_2(O)P$–DiamOH, **2**) were synthesized. After that, the metal composites Pd@PH_2–DiamOH (**3**) and Pd@$P(O)H_2$–DiamOH (**4**), were generated by low-temperature chemical vapor deposition. We found a tetragonal symmetry with strong H-bonding that leads to tetrameric arrangement. At a large-scale arrangement of the crystalline structure, a significant nanoporosity appears (Channel voids with a total volume of 168 $Å^3$ (~ 6.4% of unit cell), obtaining a high specific area (up to 140m^2/g).

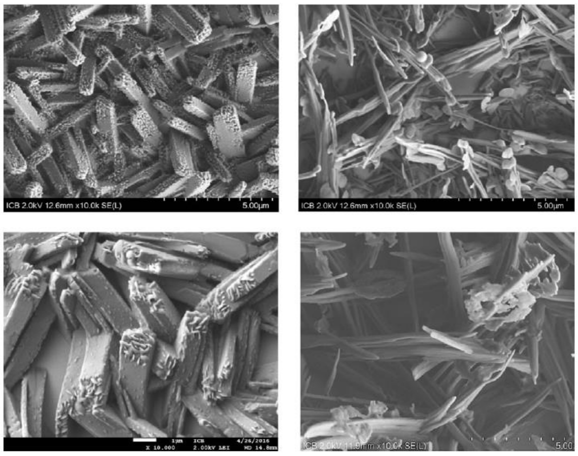

Figure 1. Scanning electron microscopy (SEM) of **1** (top left) and **2** (top right), and metal nanocomposites Pd@PH_2–DiamOH, **3** (bottom left) and Pd@$P(O)H_2$–DiamOH **4** (bottom right).

The nanolayering of palladium over self-assembled **1** and **2** led to nanocomposites **3** and **4**, respectively, for which scanning electron microscopy views are given in

Fig. 1. The self-assemblies of **1-4** were produced with high structural uniformity and reproducibility. From SEM, the diamondoid deposit thickness was estimated above 175 nm. ToF-SIMS depth profiling indicates thus a Pd nanolayer thinner than 5 nm.

3. Results

Gas sensing experiments were conducted in a 35 cm^3 airtight test chamber, with the pieces of silicon wafers glued to a miniaturized ceramic hotplate and connected to a printed circuit board. The self-assembly of diamondoid phosphine H_2P–DiamOH **1** showed a NO_2 response (3.0% at 100 ppm) slightly superior to its oxide $H_2(O)P$–DiamOH **2** (1.5% at 100 ppm) and its Pd nanocomposite Pd@PH_2–DiamOH **3** (2.1% at 100 ppm). A significant NO_2 response was achieved with metal nanocomposite Pd@$P(O)H_2$–DiamOH **4** with fast response and recovery processes (4.8% at 100 ppm). We further explored the detection limit of our systems for NO_2 in a 13 cm^3 airtight test chamber, reducing the dead volume with unchanged operating temperature (100 °C) and exposure/recovery times. Under these conditions, the detection of NO_2 concentrations from 50 to 1000 ppb was successfully achieved, and confirmed the suitability of sp^3-carbon-based sensors for detecting few ten ppb of nitrogen dioxide.

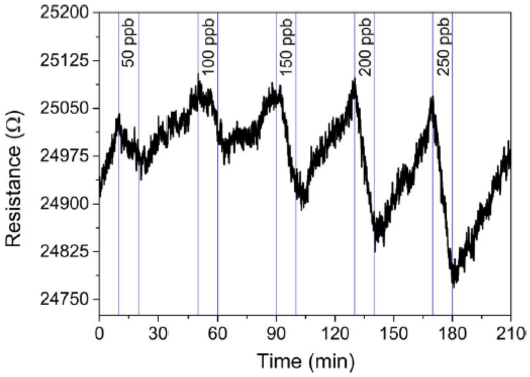

Figure 2. Example of NO_2 detection at 50–250 ppb level for sensor Pd@PH_2–DiamOH **3**.

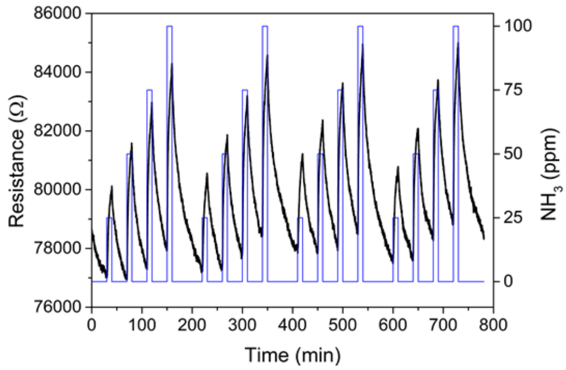

Figure 3. Example of the reversible NH_3 detection at 25, 50, 75, and 100 ppm for Pd@PH_2–DiamOH **3** material.

The same samples were used for NH_3 detection (Figure 3) showing an even higher sensitivity (>10.0% for H_2P–DiamOH **1** and >7.0% for Pd@PH_2–DiamOH **3** at 100 ppm NH_3).

An issue of low-temperature sensing is the potential interference of relative humidity and the sensitivity to water is a factor to consider for practical devices [3]. The detection of NO_2 was effective under either set of conditions (Figure 4), with different behavior still to rationalize, since **2** (and **3**) increases the sensitivity in humid atmosphere compared to dry conditions, while **4** (and **1**) performed better under dry conditions. In any case the responses were kept detectable in the same range (1–4%).

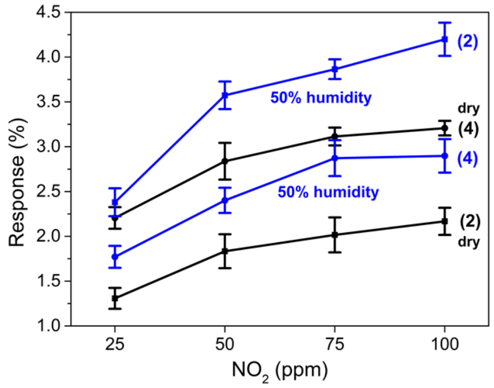

Figure 4. NO_2 response with sensors **2** and **4** in dry or humid conditions: ■ = $H_2P(O)$–DiamOH (**2**), ● = Pd@$P(O)H_2$–DiamOH (**4**) in dry conditions; ■ = $H_2P(O)$–DiamOH (**2**), ● = Pd@$P(O)H_2$–DiamOH (**4**) in humid conditions (50% relative humidity).

4. Conclusions

This work reports the first application of sp^3-C-based gas sensors. Remarkably, they tolerate humid conditions and achieve sensing of NO_2 at ppb levels at 100 °C. Pristine and metal-nanolayered diamondoids can both be gas responsive. Such gas sensing properties are related to primary phosphine-diamantanol based compounds for which channel nanoporosity (and SBet ca. 140 m^2/g) derives from H-bonding in the solid state. We aim at extending our new approach to other metals on suitably functionalized diamondoid sp^3-carbon-based nanostructures.

5. References

[1] J. Casanova-Chafer, et.al., Angew. Chem. Int. Ed. 2019, 58, 1-7.
[2] A. C. Rai, P. et. al., Sci. Total Environ. 2017, 508, 383 and related World Health Organization (WHO) annual reports cited therein.
[3] D. R. Kauffman, et.al., Angew. Chem. Int. Ed. 2008, 47, 6550.
[4] S. S. Shendage, et. al., Sens. Actuators B 2017, 240, 426.
[5] V. Schroeder, et. al., Chem. Rev. 2018, 118.

Pulsed UV Light on Au-decorated Carbon Nanotubes Gas Sensor to Determine NO2 Concentration

E. González (1, *), J. Casanova-Chafer (1), A. Romero (1), X. Vilanova (1), E. Llobet (1)

(1) Universitat Rovira i Virgili/ Department of Electronic, Electric and Automatic Engineering, Avinguda dels Països Catalans, 26, 43007 Tarragona
(*) corresponding author: ernesto.gonzalez@urv.cat

Abstract

We show that analyzing the transient response of a pulsed UV light-excited carbon nanotube sensor enables the quantification of NO_2. Fast Fourier Transform feature extraction coupled to Partial Least Squares Regression models were used. The method developed allows faster detection of NO_2 at room temperature than when standard resistive measurements are used. The method does not require a good baseline stabilization and enables savings in power consumption, since it avoids heating the sensor.

1. Introduction

Although CNTs have been widely studied as gas sensors, some challenges still remain unsolved. Measurements employing CNTs at room temperature show important drift problems and poor reproducibility. Moreover, desorption of gas molecules is a big issue (e.g., achieving a stable baseline), increasing the time needed to reliably detect gases [1]. Operated at room temperature and suddenly exposed to NO2, a CNT sensor nay not have reached the steady-state after 8 hours, and baseline recovery under dry air may not be recovered after 40 hours (see Figure 1). One alternative is to heat up the sensor surface to desorb gas molecules, increasing the power consumption [2]. Another alternative is applying UV light in the recovery phase to desorb the species attached on CNT, but this technique does not improve the response time during the adsorption phase [3].

We demonstrate that combining pulsed UV light together with FFT and PLSR analysis, makes possible quantifying NO_2 for a CNT sensor operated at room temperature, enabling low power consumption and reduced response time (quantification in just 4 minutes), since it is not mandatory to achieve steady-state or regain a stable baseline for identifying gas concentration (Figure 2).

2. Description of the method

O. Gonzalez and co-workers, reported the use of pulsed UV light on metal oxide gas sensors, obtaining the information to identify the gas concentration from the resistance change (rates) due to the light modulation [4]. Nevertheless, this approach was not useful in our case, not allowing a clear determination of the concentration (see PCA results in Figure 3a). Therefore, we have used a new signal treatment based on PLSR analysis, where the features input to the model are FFT components and observations are the different gas concentrations. The FFT component regarding to the UV light switching and its two first even order harmonics are used to construct the matrix used as input of the model. A PCA analysis employing FFT components indicates that PC1 relates to concentration (Figure 3b). We generated a training matrix with information from 7 cycles of 300, 500 and 700 ppb of NO2. A PLSR model was obtained from the training matrix, and a cross-validation mechanism was used, by mean of a leave-one-out strategy. This strategy was carried out by taking the information about the three concentrations of a cycle as validation set and the rest of information as training set. This process was repeated 7 times to test the prediction accuracy of all the training matrix. Figure 4 depicts the calibration model and cross-validation results, as well as the linear regression for both of them. The r-squared values and RMSE from the calibration model and cross-validation results were computed to analyse the prediction accuracy of the models developed.

3. Conclusions

The method described was successfully implemented for a gas sensor based on CNTs decorated with gold nanoparticles. We found an R-squared value for the calibration model of 0.9464 and for the validation of 0.9219. The RMSE from the calibration model and the validation were 36.8 ppb and 45 ppb, respectively. Since just an average of 25 mW is used to power on the UV LED, the power consumption was reduced about 93% respect to the case of heating the same sensor up to 150 ºC [2].

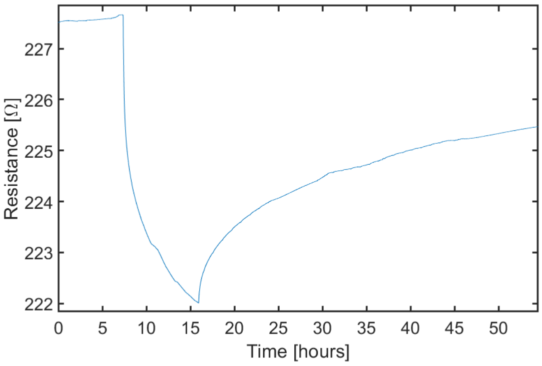

Fig.1. Long-term response to NO2 and recovery phase at room temperature of a CNT sensor.

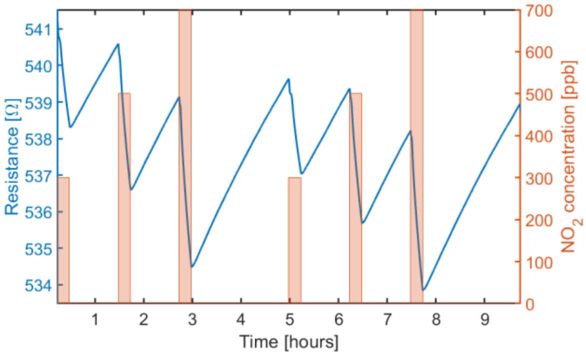

Fig.2. Sensor signal with pulsed UV light and room temperature.

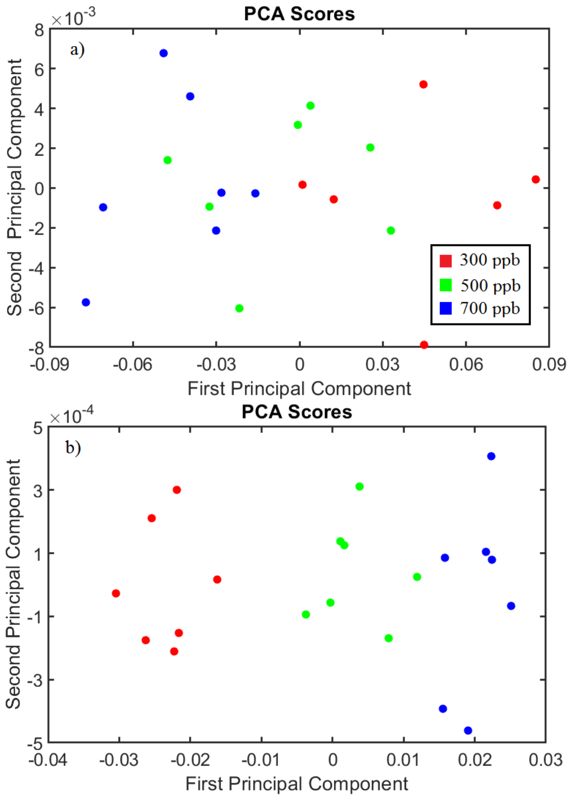

Fig.3. PCA analysis employing rates (a) and FFT components (b).

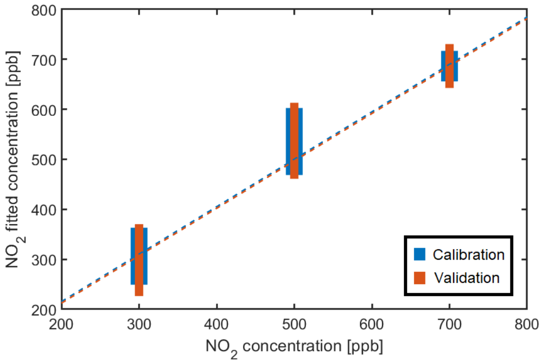

Fig.4. Calibration model and cross-validation of the training matrix.

References (Times 10 bold)

1 A. Salehi-khojin, et al, Nonthermal Current-Stimulated Carbon Nanotubes, Science, 2010, 329, 1327–1330.

2 P. R. Mudimela, et al, Gas sensing with gold-decorated vertically aligned carbon nanotubes, Beilstein J. Nanotechnol., 2014, 5, 910–918.

3 R. J. Chen, et al, Molecular photodesorption from single-walled carbon nanotubes, Appl. Phys. Lett., 2001, 79, 2258–2260.

4 O. Gonzalez, et al, Pulsed UV Light Activated Gas Sensing in Tungsten Oxide Nanowires, Procedia Eng., 2016, 168, 351–354.

Design of Nanoporous Anodic Alumina Structures with Overlapped and Stacked Photonic bands

Laura K. Acosta, Elisabet Xifre-Perez, Josep Ferré-Borrull and Lluis F. Marsal*

Departament d'Enginyeria Electrònica, Elèctric i Automàtica, Universitat Rovira i Virgili,
*Avinguda Països Catalans 26, 43007 Tarragona, Spain. *Corresponding author e-mail address: lluis.marsal@urv.*

Abstract

Nanoporous Anodic Alumina Photonic Structures are obtained by electrochemical anodization of aluminum in the appropriate conditions and by means of continuously varying anodization current. In this work, we present a comprehensive study of different photonic structures based on multiple periodic structures with sinusoidal profiles in overlapped and stacked configuration.

1. Introduction

Nanoporous anodic alumina (NAA) is a promising material formed by the electrochemical oxidation of aluminum, a cost effective and fully scalable process compatible with conventional micro and nanofabrication approaches that allows the precise control over the geometry and distribution of the pores [1-2]. The optical properties of NAA rely intrinsically upon its nanoporous architecture. Therefore, to engineer the nanoporous structure of NAA provides novel means of modulating its refractive index in a multidimensional fashion to fabricate advanced materials with unique optical properties to guide, reflect, transmit, emit, and enhance incident light The design and engineering of photonic structures with innovative architectures and materials can engineer the way for controlling light−matter interactions at the nanoscale in novel ways. These nanostructures would enable new opportunities to develop advanced materials for many applications, including optical chemical sensing and biosensing. [3-4].

2. Materials and Methods

Materials

High purity Aluminium foils (thickness 0.5 mm and purity 99.99%), Ethanol (C_2H_5OH), perchloric acid ($HClO_4$), oxalic acid ($H_2C_2O_4$), hydrochloric acid (HCl), copper chloride ($CuCl_2$) were purchased from Sigma-Aldrich. Double deionized water (DI) (18.6 MΩ) was used for all the solutions unless other specified.

Fabrication

First Al substrates were degreased in acetone, cleaned with ethanol and DI water and finally dried under steam of air. Before the anodization, Al substrates were electropolished in a mixture of ethanol and perchloric acid 4:1 at 20 V and 5ºC for 5 min. During the electropolishing step the stirring direction was alternated every 60 s. After the electropolishing the samples were cleaned with ethanol and DI water and dried under steam of air [4]. Then, the anodization was carried out in $H_2C_2O_4$ 0.3 M at 5ºC applying a sinusoidal current profile with several design parameters like offset current (I0), amplitude current (I1), Period (T) and number of periods (N). Multiple periodic currents are applied sequentially instead of simultaneously. In this work, different photonic structures are overlapped and stacked on the same structure. This permits to use a bigger current contrast in the current variations and using electrolytes with different composition. Figure 1 shows the sinusoidal current profile and i in stack configuration and 2 shows the sum of sinusoidal waves (overlapped configuration).

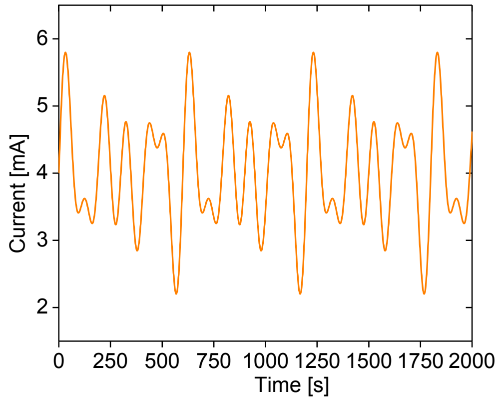

Figure 1. Current profile in overlapped configuration of NAA-Photonic structures based on nanoporous anodic alumina

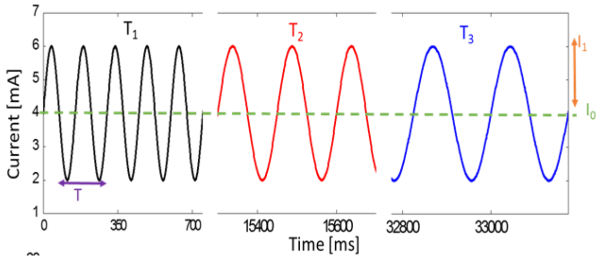

Figure 2. Current profile in stack configuration of NAA- Photonic structures based on nanoporous anodic alumina and involved fabrication parameters

3. Results

Figure 3 shows the reflectance spectrum in overlapped configuration of the described sample after removing the remaining aluminum. As it can be seen, the sum of three sinusoidal currents give rise to the formation of three stop bands. The height of these stop bands reaches between 9 % and 18 % while its widths are between 15 nm and 20 nm. It can be observed that there is a direct relationship between the period of the anodization current and the corresponding central wavelength, λ_1 = 320 nm of T_1 = 100 s, λ_2 = 520 nm of T_2 = 150 s, λ_3 = 700 nm of T_3 = 200 s.

Figure 4 shows the reflectance spectrum in stack configuration after removing the remaining aluminum. Three successive sinusoidal currents give rise to the formation of three stop bands. The height of these stop bands reaches between 18 % and 39 % while its widths are between 20 nm and 25 nm. It can be observed that there is a direct relationship between the period of the anodization current and the corresponding central wavelength, λ1 = 320 nm of T1 = 100 s, λ2 = 420 nm of T2 = 125 s, λ3 = 520 nm of T3 = 150 s.

The effects of fabrication parameters are systematically assessed, revealing that the positions of the characteristic bands of these photonic structures are highly controllable.

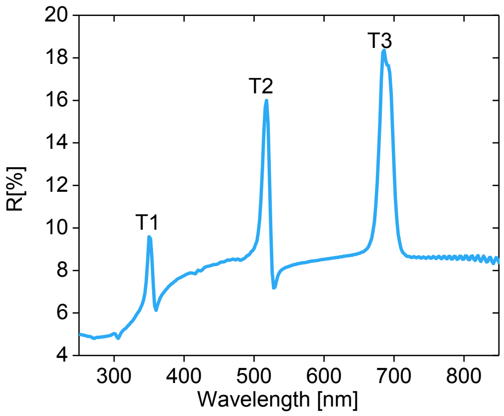

Figure 3. Reflectance spectra of Nanoporous Anodic Alumina Photonic Structures samples with different period time (T) in overlapped configuration.

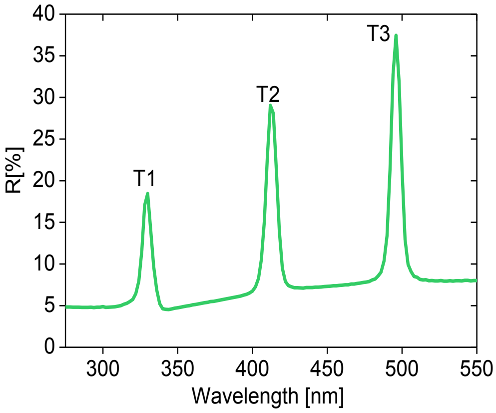

Figure 4. Reflectance spectra of Nanoporous Anodic Alumina Photonic Structures samples with different period time (T) in stack configuration.

4. Conclusions

In this work we demonstrate the possibility to fabricate Photonic Structures based in Nanoporous Anodic Alumina in overlapped and stack configuration by the application of the sum and successive sinusoidal anodization currents respectively with different period time. The position of the forbidden bands presented by these photonic structures based on nanoporous anodic alumina can be accurately tuned by varying the anodization period of the anodization current density waveform. The effects of fabrication parameters are systematically assessed, revealing that the positions of the characteristic forbidden bands of Photonic structures are highly controllable.

Acknowledgements

This work was supported by the Spanish Ministerio de Ciencia, Innovación y Universidades (MICINN/FEDER) RTI2018-094040-B-I00, by the Agency for Management of University and Research Grants (AGAUR) ref. 2017-SGR-1527 and by the Catalan Institution for Research and Advanced Studies (ICREA) under the ICREA Academia Award

References

[1] J. Ferre-Borrull, J. Pallares, Macías G, L.F. Marsal, Materials. 7 (2014). 5225-5253

[2] G. Macias, L.P. Hernández-Eguía, J. Ferré-Borrull, J. Pallares, L.F. Marsal, ACS Appl. Mater. Interfaces, 5 (2013) 8093.

[3] T Kumeria, A Santos, MM Rahman, J Ferré-Borrull, LF Marsal, D Losic, ACS Photonics 1 (2014), 1298-1306

[4] Laura K. Acosta, Francesc Bertó-Roselló, E. Xifre-Perez, Abel Santos, J. Ferre-Borrull, L.F. Marsal. ACS Appl. Mater. Interfaces, 11, (2019). 3360-3371

Analytical Model for VT Shift in Submicron Staggered Organic TFTs

Jakob Prüfer[1,2,✠], Jakob Simon Leise[1,2], Ghader Darbandy[1], James W. Borchert[3,4], Hagen Klauk[3],
Benjamín Iñíguez[2], Thomas Gneiting[5] and Alexander Kloes[1]
[1]NanoP, TH Mittelhessen University of Applied Sciences, Giessen, Germany,
[2]DEEEA, Universitat Rovira i Virgili, Tarragona, Spain,
[3]Max Planck Institute for Solid State Research, Stuttgart, Germany,
[4] Functional Polymers, Institute of Polymer Chemistry, Universität Stuttgart, Germany,
[5]AdMOS GmbH, Frickenhausen , Germany,
✠jakob.pruefer@ei.thm.de

***Abstract*—This paper presents a compact model for the threshold-voltage shift, consisting of $V_{T,roll-off}$ and Drain-Induced-Barrier-Lowering (DIBL), in short-channel staggered organic thin-film transistors (OTFTs). An analytical surface potential solution is derived for a staggered geometry containing two-dimensional effects which is used to extract the $V_{T,roll-off}$ and DIBL out of it. Thus, the closed-form and physics-based equations extend an existing compact current model by incorporating them into expressions for V_T. Verification of the modeling approach is done by comparison with TCAD Sentaurus simulations as well as measurements on organic TFTs with a channel length down to 400 nm.**

I. INTRODUCTION

The low on-state current of organic semiconductor must increase to make them promising options for radio-frequency operations [1]. Although their charge-carrier mobility has been increased continuously, a channel length reduction is additionally necessary. As soon as the channel length reaches the submicron range, the measurements and TCAD simulations show a threshold voltage reduction, well known as threshold voltage roll-off $V_{T,roll-off}$ in short-channel MOS transistors [2]. Moreover, TCAD simulations show an increasing DIBL effect and subthreshold slope degradation for short-channel OTFTs. This work introduces a closed-form analytical approach for calculating $V_{T,roll-off}$ and DIBL depending on the geometry and bias conditions for staggered OTFT structures as published in [1].

II. MODELING APPROACH

A. Surface Potential Solution

For the calculation of both effects, $V_{T,roll-off}$ and DIBL, a solution of the Laplace equation is necessary whereof the barrier height in the channel can be extracted. Fortunately, the staggered geometry makes it possible to adapt an existing potential solution of a similar structure presented in [3]. There, the potential problem is split into two problems with different boundary conditions based on the original boundaries as in Fig. 1.

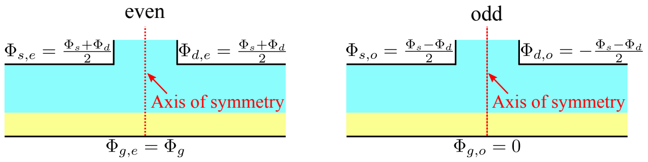

Figure 1. Even- and odd-mode potential problem with the decomposition of the original boundary conditions.

Both solutions superposed yield the actual potential solution with the original boundary conditions. Thus, the derivation is much simpler since the boundary conditions make it possible to deduce only one half of the OTFT to calculate the whole device. Subsequently, the Schwarz-Christoffel-Transformation [4] is applied to create a mapping function which transforms the upper half of a complex w-plane upon a region of interest in a complex z-plane, which corresponds to one half of the model structure as in Fig. 2 (hatched domain).

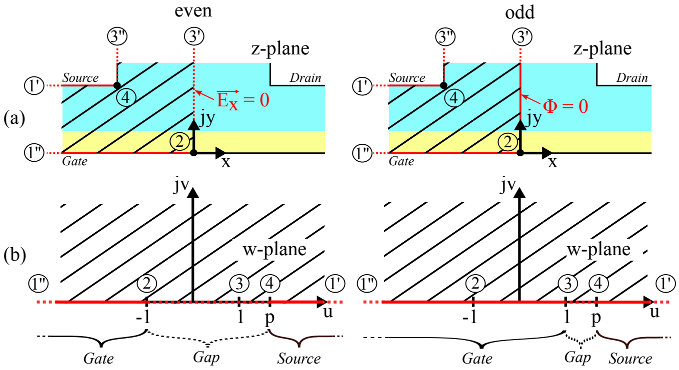

Figure 2. (a) Original geometry (hatched) in z-plane and (b) the corresponding geometry in w-plane wherein the electric field solution is calculated.

Since the Laplace equation is invariant to conformal mapping, an existing general electric field solution [4] of a similar geometry as in Fig. 2(b) was used to derive an electric field solution of even- and odd-mode in z-plane. Assuming that the accumulation channel is very close to the gate dielectric and the electric field $E_{die}(u)$ is constant through it, the voltage drop across the gate-dielectric can be calculated with the gate-dielectric thickness. This enables to derive the surface potential

---

The project was funded by the German Federal Ministry of Education and Research ("SOMOFLEX", No. 13FH015IX6), EU H2020 RISE ("DOMINO", No. 645760), and the German Research Foundation (DFG) under the grant KL 1042/9-2 (SPP FFlexCom).

solution since the gate boundary condition Φ_g is known:

$$\Phi_{surf}(u) = \Phi_g - E_{die}(u) \cdot d \cdot \frac{\epsilon_{osc}}{\epsilon_{die}}. \tag{1}$$

where the fitting parameter $d = t_{die}$ defines the position of the surface potential cutline, ϵ_{osc} the relative permittivity of the organic semiconductor and of ϵ_{die} the relative permittivity of the gate-dielectric. In case of the $V_{T,roll-off}$ model the extraction of the barrier is done in the middle of the channel. In case of the DIBL model Fig. 3 shows that an extraction in the middle of the channel is sufficient. Finally, following expression are derived by applying eqn. (1) for both models:

$$\Delta V_{T,roll-off} = \alpha\left(\Phi_g - \frac{\Phi_s + \Phi_d}{2}\right)\frac{\pi d}{t_{die}\epsilon_{osc}/\epsilon_{die} + t_{osc}} \cdot \frac{2}{p+1}, \tag{2}$$

$$\Delta V_{DIBL} = \alpha \frac{V_{ds}}{p+1} \cdot \frac{\pi d}{t_{die}\epsilon_{osc}/\epsilon_{die} + t_{osc}} \tag{3}$$

with the thickness of the gate-dielectric t_{die} and organic semiconductor t_{osc} and eventually the parameter p is given by:

$$p = 1 + \frac{L_{ch}^2}{2\pi^2 C^2} \quad with \quad C = -\frac{t_{die}\epsilon_{osc}/\epsilon_{die} + t_{osc}}{\pi}. \tag{4}$$

The parameter α defines the subthreshold slope degradation and is extracted from eqn. (1):

$$\alpha = \frac{dV_g}{\Phi_{surf,max}(V_{fb} + dV_g) - \Phi_{surf,max}(V_{fb})}. \tag{5}$$

III. RESULTS AND VERIFICATION

A. DIBL Effect

In section II it has been mentioned that the calculation of the exact position of the barrier maximum is not necessary for the calculation of the DIBL effect, and hence a potential extraction by eqn. (1) in the middle of the channel is sufficient.

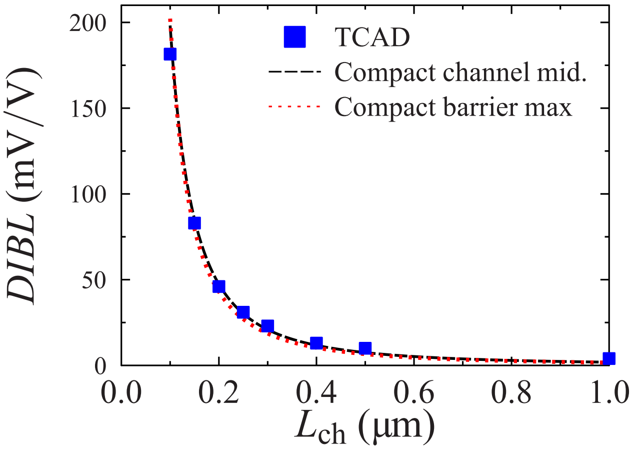

Figure 3. Fitted compact model with potential extraction in channel middle and at actual barrier maximum compared with TCAD simulations of devices with $t_{die} = 5.1\,\mathrm{nm}$ and $t_{osc} = 25\,\mathrm{nm}$ regarding channel length.

This was checked by an iterative algorithm which determines the barrier maximum position and thus enables to calculate the DIBL including the shift of the barrier maximum. Figure 3 shows that the extraction of the DIBL yields almost identical results for both methods. The DIBL has been extracted using the drain voltages $V_{ds1} = -0.1\,\mathrm{V}$ and $V_{ds2} = -1.5\,\mathrm{V}$. An oxide thickness $t_{die} = 5.1\,\mathrm{nm}$ and OSC thickness of $t_{osc} = 25\,\mathrm{nm}$ was taken for the geometry of the devices.

B. Threshold Voltage Roll-off $V_{T,roll-off}$

The same TCAD simulations as for the verification of the DIBL effect in section III-A have been used to verify the $V_{T,roll-off}$. It is important to mention that the $V_{T,roll-off}$ for the OTFT with a channel length of $L_{ch} = 1\,\mu\mathrm{m}$ is used as a reference for all other values to allow all data to be compared. With a fitting parameter $d = 0.8 \cdot t_{die}$ the $V_{T,roll-off}$ model shows in Fig. 4 very good agreement with the TCAD simulations. In addition to TCAD simulation data, OTFTs with different channel lengths between 400 nm and 1 µm but a constant W/L_{ch} ratio have been fabricated at the Max-Planck-Institute in Stuttgart. Measurements clearly show a $V_{T,roll-off}$. The threshold voltage V_T for the five OTFTs has been extracted using the transfer characteristic in the linear regime and the constant current method. Results of both methods differ only slightly and are shown in Fig. 4 as reference.

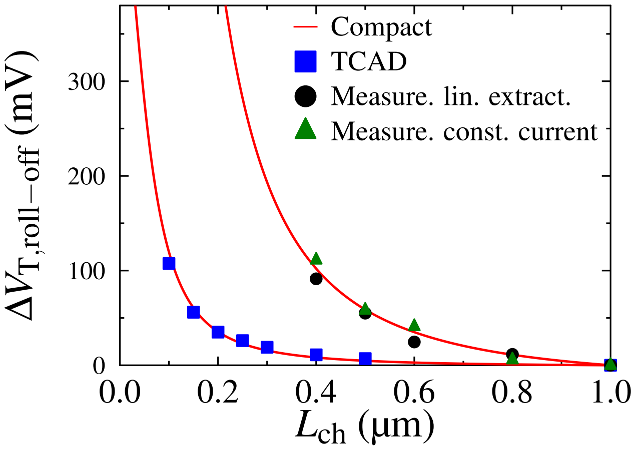

Figure 4. $V_{T,roll-off}$ model fitting vs. TCAD simulations of devices with $t_{die} = 5.1\,\mathrm{nm}$ and $t_{osc} = 25\,\mathrm{nm}$ as well as measurements extracted on two different methods regarding channel length.

REFERENCES

[1] U. Zschieschang, J. W. Borchert, M. Geiger, F. Letzkus, J. N. Burghartz, and H. Klauk, “Stencil lithography for organic thin-film transistors with a channel length of 300 nm,” *Organic Electronics*, vol. 61, pp. 65–69, Oct 2018.

[2] N. Arora, “MOSFET Modeling for VLSI Simulation”, *World Scientific Publishing Company*, 2007.

[3] D. Freund, A. Kloes, A. Kostka, “Conformal mapping techniques for the analytical, two-dimensional calculation of currents in lateral bipolar transistor structures”, *Solid-State Electronics*, Vol. 39, No. 4, pp. 529–540, 1996.

[4] E. Weber, “Electromagnetic Fields - Theory and Applications, Volume I Mapping of Fields.” *John Wiley & Sons, Inc.*, New York, 1950.

Ion migration and carrier recombination kinetics revisited

Jesús Jiménez-López[1,2] and Emilio Palomares[1,3]

1. Institute of Chemical Research of Catalonia (ICIQ). The Barcelona Institute of Science and Technology (BIST), Av. Països Catalans 16, 43007, Tarragona, Spain
2. Departament d'Enginyeria Eletrònica, Elèctrica i Automàtica (DEEEA), Universitat Rovira i Virgili (URV), Av. Països Catalans 26, 43007, Tarragona, Spain
3. Catalan Institution for Research and Advanced Studies (ICREA), Passeig Lluís Companys 23, 08010, Barcelona (Spain)

Abstract

In Perovskite Solar Cells, the reduction of interfacial carrier recombination is key in order to increase device efficiencies. It has been demonstrated that the characteristic ionic motion on these devices has a direct relationship over carrier recombination. Here, we have observed how this influence varies with the aging of the devices. This signal changes with time, and we have assigned this behavior to a better/faster ion distribution within perovskite material.

1. Introduction

Finding the major carrier losses is key to gain better efficiencies in Perovskite Solar Cells (PSC)[1]. Different techniques, performed in films[2,3] or working devices[4,5], have been used to study carrier recombination in PSC. From the different types of carrier recombination in PSC[6,7], it has been suggested that one of the major carrier losses is associated with carrier recombination at the interfaces.

Transient Photovoltage (TPV) has been used to study carrier recombination in solar cell devices. In this technique, the device is illuminated and kept at open circuit conditions, so, a photovoltage is generated. Additionally, a laser pulse generates an extra number of carriers, which are forced to recombine as the device continues in open circuit conditions.

A modification of this technique, called "transient of the transient" described by Calado et al.[8] and Pockett et al.[9] have been very useful to understand better ion migration in PSC. They studied the evolution of the TPV perturbations as the Voc of the solar cell stabilizes. The stabilization of the Voc in perovskite solar cells normally takes long times (up to hundreds of seconds), what has been assigned to the presence of ions at the perovskite interface in dark conditions and their redistribution when light irradiates the device[10]. From this technique, negative transient deflections appear that are correlated with ionic accumulation at the interfaces of the device.

In this research, we have seek further on the disappearance of this negative transient and analyzed how the signal changes in correlation with the device aging and its relation with the hysteresis and the increase in the Voc values of the triple cation PSC, $Cs_{0.1}(FA_{0.85}MA_{0.15})Pb(I_{0.85}Br_{0.15})_3$, herein referred as CsFAMAPbIBr (FA = $CH(NH_2)^{2+}$; MA = $CH_3NH_3^+$). For this purpose, the solar cells were stored in N_2 first and later on in air conditions with controlled humidity (<10 % H_2O).

2. Results and Discussion

We prepared PSC with TiO2, both compact and mesoporous layer as Electron Transport Material (ETM), and spiro-OMeTAD as Hole Transporting Material (HTM). The devices were measured for 45 days, and, for the sake of clarity, we only show results from days 3 and 45 (Figure 1).

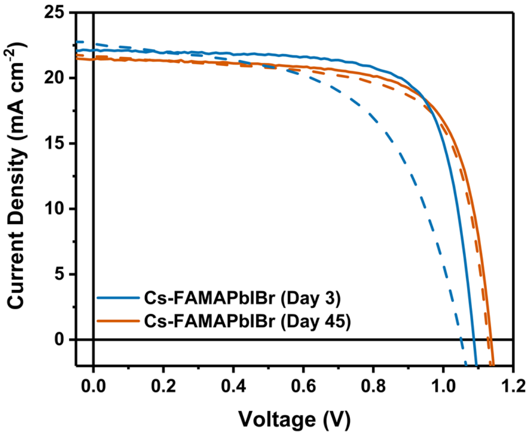

Figure 1. JV curves of the same device measured on day 3 and day 45 at 1 Sun conditions (AM 1.5G, 100 mW/cm2) and a scan rate of 40 mV/s.

The most remarkable feature is the reduction of the hysteresis observed after the storage of the solar cells in air conditions (<10 % H_2O). It is also quite remarkable the increase in Voc values after the aging process, which suggest a reduced carrier recombination over time. About hysteresis, ionic accumulation at the interfaces has been attributed as one of the main responsible for this effect. In order to estimate its influence on carrier recombination, we measure TPV at the early stages of illumination, when the ions have not enough time to reorganize inside the cell.

TPV transients at early illumination times show a clear negative deflection, which is associated with an increase recombination at the interfaces (Figure 2A). This behavior is associated with accumulated ions at the interface. They will move to compensate the photogenerated electric field, but they do it slowly, so, as far as they continue at the interfaces, its associated electric field will drive carriers in the opposite direction of extraction. Thus, increasing carrier recombination and obtaining lower voltages. For our surprise, aged devices do not show this negative transient deflection (Figure 2B), which is associated with a faster/better ionic reorganization. Therefore, the ionic influence on carrier recombination is reduced. This would explain also the reduced hysteresis on these devices.

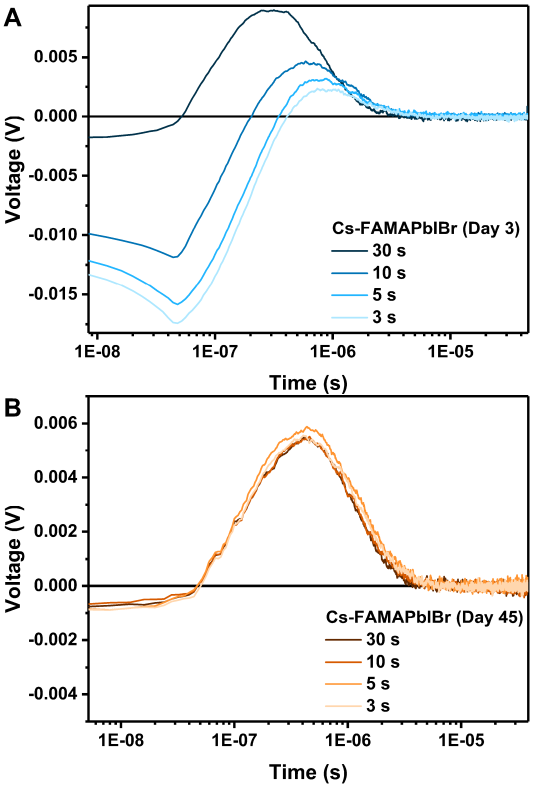

Figure 2. (A) The TPV signals of the device measured on Day 3 with different illumination times. (B) The TPV signals of the device measured on Day 45 with different illumination times.

3. Conclusions

In conclusion, we have fabricated PSC that in a first approach showed a higher degree of hysteresis, decreasing over different measurement days when they were stored in air conditions. These devices were characterized using advanced transient techniques, such as TPV, CE, and TPC that give us information about carrier recombination in the PSC. From this analysis, we conclude that the influence of ion migration over the carrier recombination is reduced over different measurement days. As a consequence, an increased Voc and fill factor in the devices is observed, with the concomitant decrease of carrier losses due to recombination.

Acknowledgements

We thank MINECO (projects CTQ2013-47183 and CTQ 2017-89814-P). EP is also thankful to ICIQ and ICREA for economical support.

References

1 J. P. Correa-Baena, W. Tress, K. Domanski, E. H. Anaraki, S. H. Turren-Cruz, B. Roose, P. P. Boix, M. Grätzel, M. Saliba, A. Abate and A. Hagfeldt, *Energy Environ. Sci.*, 2017, **10**, 1207–1212.

2 Z. Liu, L. Krückemeier, B. Krogmeier, B. Klingebiel, J. A. Márquez, S. Levcenko, S. Öz, S. Mathur, U. Rau, T. Unold and T. Kirchartz, *ACS Energy Lett.*, 2018, **7**, 110–117.

3 S. D. Stranks, G. E. Eperon, G. Grancini, C. Menelaou, M. J. P. Alcocer, T. Leijtens, L. M. Herz, A. Petrozza and H. J. Snaith, *Science*, 2013, **342**, 341–344.

4 J. Jiménez-López, W. Cambarau, L. Cabau and E. Palomares, *Sci. Rep.*, 2017, **7**, 6101.

5 A. Pockett, G. E. Eperon, T. Peltola, H. J. Snaith, A. Walker, L. M. Peter and P. J. Cameron, *J. Phys. Chem. C*, 2015, **119**, 3456–3465.

6 A. Marchioro, J. Teuscher, D. Friedrich, M. Kunst, R. Van De Krol, T. Moehl, M. Grätzel and J.-E. E. Moser, *Nat. Photonics*, 2014, **8**, 250–255.

7 W. Tress, M. Yavari, K. Domanski, P. Yadav, B. Niesen, J. P. Correa Baena, A. Hagfeldt and M. Graetzel, *Energy Environ. Sci*, 2018, **11**, 151.

8 P. Calado, A. M. Telford, D. Bryant, X. Li, J. Nelson, B. C. O'Regan and P. R. F. F. Barnes, *Nat. Commun.*, 2016, **7**, 13831.

9 A. Pockett and M. J. Carnie, *ACS Energy Lett.*, 2017, **2**, 1683–1689.

10 A. Pockett, G. E. Eperon, N. Sakai, H. J. Snaith, L. M. Peter and P. J. Cameron, *Phys. Chem. Chem. Phys.*, 2017, **19**, 5959–5970.

Fabrication of One Dimensional Nanoporous Anodic alumina structures using electrochemical anodization

Pankaj Kapruwan, Josep Ferré-Borrull*, Lluís F. Marsal*

Engineering. Electrònica, Elèctrica i Automàtica, Universitat Rovira i Virgilli, 43007, Tarragona, Spain

*Email: josep.ferre@urv.cat, lluis.marsal@urv.cat

Abstract

Recent years have seen potential growth in ordered Nanoporous anodic alumina (NAA) structures due to inexpensive and scalable production by simple electrochemical anodization processes. This self-organized hexagonal nanostructure arrangement can widely be tuned with different surface chemistries and properties to exploit a range of applications such as bio-sensing, drug delivery, separation and electronics. In this paper, two different types of anodization regimes (Galvanostatic and potentiostatic) were explored. Anodization was performed under two different electrolytes: 0.3 M sulphuric acid and 0.3 M Oxalic acid. Environmental Scanning electron microscopy (ESEM) was used to identify the structural characteristics (pore diameter, inter-pore distance and cross section). It is shown that by varying anodization modes and parameters, several types of One Dimensional (1D) nanostructures can be fabricated.

1. Introduction

The two step anodization process developed by Masuda et al in 1995 [1], revolutionized the nanotechnology growth to a great extent, specifically in the area of Nanoporous Anodic Alumina (NAA) as pores obtained with this procedure were perfectly hexagonally arranged array structure. This procedure involved formation of first oxide layer in potentiostatic mode which is selectively etched by chemical etching followed by growing of second oxide layer to form ordered hexagonal patterns. This form of anodization at low voltage referred to as "mild anodization" process. Although, the process results in highly ordered NAA structures but the main disadvantage lied in prolonged duration of the procedure. Therefore, more fast and efficient approach towards fabrication was introduced at high voltages widely known as hard anodization was introduced by Lee et al. [2]. In addition, several protocols has already been developed so far [3, 4].

Taking advantage of these two pre-existing procedures, Lee et al developed another interesting approach combining Mild Anodization (MA) and Hard anodization (HA) conditions, where duration of the pulse dominates the length of alumina nanotubes [5].

In this study, we have demonstrated the fabrication of ordered one Dimensional (1-D) nanostructures at low and high voltages. The two step anodization process was carried out in oxalic acid under controlled temperature to form long ordered porous structures. On the other hand, pulse anodization was performed in sulphuric acid to obtain Alumina nanotubes. The study can be particularly useful for growth of NAA in several applications.

2. Experimental section

Materials: High purity aluminium discs (Al) (thickness, 0.5 mm and purity 99.99 %) were purchased from Good fellow Cambridge ltd. (U.K.), acetone ($(CH_3)_2CO$), ethanol (C_2H_5OH), perchloric acid ($HClO_4$), oxalic acid ($H_2C_2O_4$), sulfuric acid(H_2SO_4), Phosphoric acid (H_3PO_4), Chromic acid (H_2CrO_4), Hydrochloric acid (HCl), copper chloride ($CuCl_2$) were provided by Sigma Aldrich. Double deionized water (DI) (18.6 MΩ) was used for all the solutions unless otherwise specified.

Fabrication: In potentiostatic mode, aluminium discs were degreased with acetone and cleaned with Double deionized water in order to remove all the impurities. The exposed area to anodization was around 1.5 cm^2. Before anodization, aluminium substrates were electropolished in a mixture of 4:1 v/v of ethanol-perchloric acid at 20 V and 5 °C for 10 min, with the stirring direction alternated every 1 minute. The first step was carried out under 0.3 M Oxalic acid at 40 V for 20 hours at 6 °C. The substrates were then immersed in a solution of H_3PO_4 6% wt. and H_2CrO_7 1.8% wt. at 70°C for 3 hours to remove oxide layer. The second anodization step was carried out under same conditions as the first one except the process was controlled by charge instead of current density. The total charge (Q) of 20 C per sample was applied until desired thickness was achieved.

In Galvanostatic mode, Nanoporous anodic Alumina tubes (NAATs) were synthesized by modified galvanostatic method. In brief, aluminium discs with area of 1.4 cm^2 were degreased with acetone and cleaned with Double deionized water in order to remove all the impurities. Aluminium discs were electropolished in a mixture of 4:1 v/v of ethanol-perchloric acid at 20 V and 5 °C for 10 min with alternating change in stirring direction every 60 s. The first step was carried out under 0.3 M H_2SO_4 at 25 V for 20 hours at 6 °C. After this, pulse anodization was performed under Galvano static conditions where combination of Mild anodization (MA) and Hard Anodization (HA) pulses were provided to the substrates. In this study, we used a 5s MA pulse at a current density of 4.28 mA/cm^2 followed by 2s HA pulse of 320 mA/cm^2. Pulse anodization was performed under 0.3 M H_2SO_4 in 10 % ethanol at 1° C. The procedure was repeated for 30-60 cycles. Afterwards, remaining aluminium substrate was removed in a chemical mixture of 0.2 M $CuCl_2$ and 6.1 M HCl. To obtain the liberated nanotubes, samples were treated with gentle ultra-sonication treatment for 60 minutes.

3. Results and Discussion

Fig 1 demonstrates the current-density time (j-t) curves for two step anodization process conducted under 0.3 M oxalic acid at 40 V. As, shown, the value of current density is higher for 2nd Step as compared to the 1st Step. This difference can be explained in terms of patterning on the aluminium substrate after removal of aluminium oxide through etching.

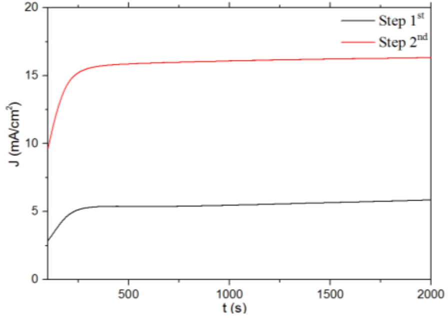

Fig 1. Typical current density profile obtained after anodization in 0.3 M oxalic acid.

The ESEM image to analyze pore size, distribution and cross section are shown. An ordered arrangement of pores with 30-35 nm can be seen from the ESEM image with the inter-pore distance of 100 nm (Fig 2, a). To analyze the structure in more detail, cross section has also been analyzed for the samples and the depth of the nanotube arrays was found to be 100 µm (Fig 2, b).

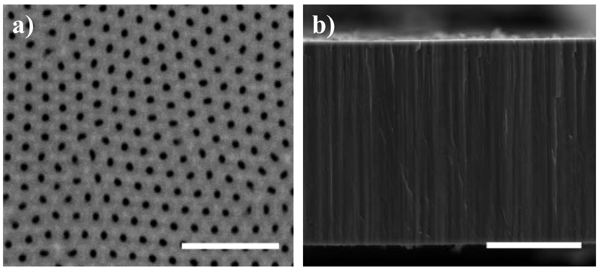

Fig 2. a) ESEM image of top view of NAA, Scale bar = 500 nm; b) Cross sectional view of NAA, Scale bar = 50 µm.

Typical anodization profile of AANTs fabricated through pulse anodization process, which is a combination of MA and HA pulses (Fig 3 a). A recovery effect was observed for HA pulses where voltage increases for a short period then attain minimum value due to formation of barrier oxide layer formed by previous pulse [5].Cross sectional ESEM image of as fabricated AANTs with layered structures. The anodization parameters were set to obtain a length of 654 ± 70 nm. After chemical etching treatment for removal of aluminium and gentle sonication for 1 hour, the layered structure was broken down into individual nanotubes structure. Fig 3, c and d, shows TEM and ESEM images of liberated nanotubes with average outer diameter of 72 nm ± 6.29 nm and inner diameter of 29 nm ± 3.7 nm.

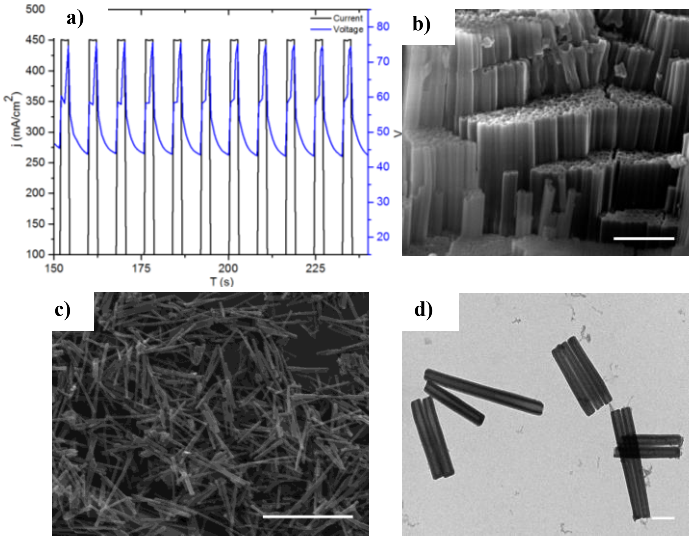

Fig 3 a) Typical current voltage profile used in Galvano static mode; b) Cross sectional image of NAA template before sonication, scale bar = 2 µm; c) Top view image of AANTs, scale bar = 5 µm; d) TEM image, scale bar = 500 nm.

4. Conclusions

In summary, electrochemical anodization is an easy and reliable way to obtain different 1D nanostructures. Due to their unique pore dimensions, tuned structural properties, these types of nanostructures offers a great possibility to be used in several applications such as sensing, catalysis, separation, electronics and drug delivery.´

5. Acknowledgement

This work was partially supported by the Spanish Ministerio de Ciencia, Innovación y Universidades (MICINN/FEDER) RTI2018-094040-B-I00, by the Agency for Management of University and Research Grants (AGAUR) ref. 2017-SGR- 1527 and by the Catalan Institution for Research and Advanced Studies (ICREA) under the ICREA Academia Award.

6. References

[1] H. Masuda and K. Fukuda, *Science (80)*, vol. 268, no. 5216, pp. 1466–1468, Jun. 1995.
[2] W. Lee, R. Ji, U. Gösele, and K. Nielsch, *Nat. Mater.*, vol. 5, no. 9, pp. 741–747, 2006.
[3] A. Santos, J. Ferré-Borrull, J. Pallarès, and L. F. Marsal, *Phys. status solidi*, vol. 208, no. 3, pp. 668–674, Mar. 2011.
[4] A. Santos, P. Formentín, J. Pallarès, J. Ferré-Borrull, and L. F. Marsal, *J. Electroanal. Chem.*, vol. 655, no. 1, pp. 73–78, 2011.
[5] W. Lee, R. Scholz, and U. Gösele, *Nano Lett.*, vol. 8, no. 8, pp. 2155–2160, 2008.

CVD growth of two-dimensional semiconducting transition metal Dichalcogenides for Gas Sensing application

A. Alagh, F.E. Annanouch, E. Llobet
MINOS-EMaS, Universitat Rovira i Virgili, Tarragona, Spain
alagh.aanchal@urv.cat, fatimaezahra.annanouch@urv.cat, eduard.llobet@urv.cat

Abstract

Recently layered inorganic material analogues to graphene such as two-dimensional transition metal dichalcogenides (2D TMDs) have emerged as promising materials for the gas sensing industry as they show promising semiconducting properties, tunable band gap, large surface area and excellent gas adsorbing capacities. Herein, we report on single step synthesis of 2D thin sheets of WS_2 and MoS_2-MoO_2 via hydrogen free, atmospheric pressure CVD technique, directly on silicon oxide substrate. E-SEM, EDX and Raman spectroscopy were used to investigate the morphology and composition of the grown material. One of these materials has been studied towards nitrogen dioxide detection, which is one among the pollutant gases present in the environment. Gas sensing results show that WS_2 is sensitive to small concentration of the gas at quite low operating temperatures.

Keywords—TMDs, APCVD, WS_2 Gas sensors, NO_2 gas, NH_3 gas, H_2S gas

1. Introduction

Two-dimensional (2D) materials are showing great potential in gas sensing with high sensitivity and providing interesting new possibilities for sensor processing. These next-generation materials consist of a metal atomic layer sandwiched between two atomic layers of a chalcogen material where the layers are stacked one above the other by Van der waals forces of interaction. Among various 2D TMDCs materials available, MoS_2 and WS_2 have attracted major attention as they offer high compatibility for integration with conventional Si technology showing superior semiconducting properties. Among the different top-down and bottom-up approaches available, Chemical Vapor Deposition (CVD) growth is the one chosen by researchers for the synthesis of 2 D materials, as it offers high surface coverage of the substrate material. CVD is a technique that allows deposition of one or more material on the substrate from volatile precursors that are caused to react by heating and hence this technique is chosen here for the deposition of thin films [1].

In this work, we report on growing 2D thin sheets of WS_2 and MoS_2-MoO_2 by a single step hydrogen free atmospheric pressure CVD technique. It is observed that the growth is highly influenced by various growth parameters such as distance between the precursors, their concentration, position of the substrate, temperature inside the growth chamber, gas flow rate and deposition time. Hence, several depositions were tried to optimize these parameters until a continuous film of the material is achieved. A WS_2 based sensor has been studied towards the detection of NO_2. We have observed impressive results for the WS_2 sensor where the sensor exhibits a good sensitivity upon exposure to small concentration (200 ppb) of NO_2 gas.

2. Results

Figure 1 depicts formation of thin films, grown at 900°C comprising of triangular domains of WS_2 with an average size of ~6µm and energy dispersive X-ray analysis also confirms the presence of W with S in the deposited layers, with an atomic ratio of 72.27 and 27.73 at %, respectively. The fine triangular shape with clean surface and smooth edge indicates growth of high quality WS_2. Raman spectrum plays a key role to identify the number of layers present, figure 2 corresponds to the Raman spectrum obtained, and here the strongest peak at~419 cm^{-1} corresponds to presence of multilayers of WS_2. Next, figure 3 shows formation of rhomboidal shaped vertically aligned large assembly of MoS_2-MoO_2 domains which are grown at 800°C. The presence of MoS_2 along with MoO_2 was also confirmed by energy dispersive X-ray analysis with an atomic ratio of 5.14, 1.18 and 40.72 of Mo, S and O at % respectively. Also, Raman spectrum obtained, figure 4 confirms the formation of MoS_2-MoO_2, where the peak at 406, 380 cm^{-1} corresponds to MoS_2 while peaks at 125,203,228,348,361,456,493,566,740 cm^{-1} confirms the presence of MoO_2 along with MoS_2 [1]. Furthermore, figure 5 shows the gas sensing results of WS_2 sensor for detection of nitrogen dioxide. Results show that the sensor exhibits a good sensitivity upon exposure to smaller concentrations of NO_2 gas with a detection limit of 50ppb.

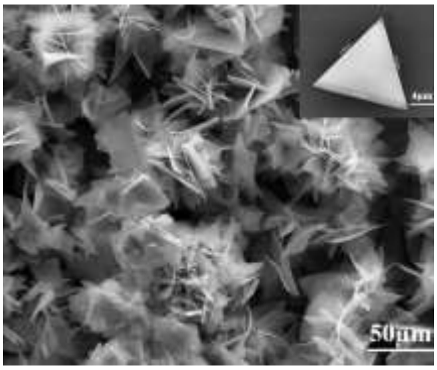

Fig. 1 ESEM image of the WS_2 thin film

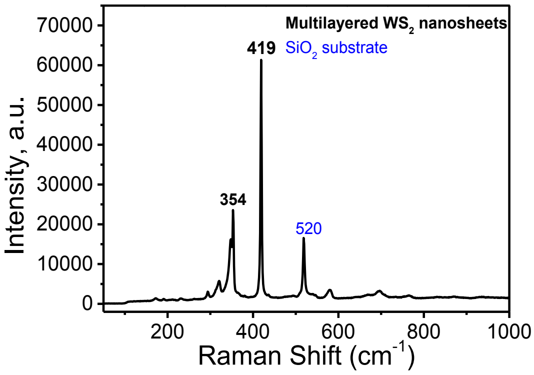

Fig. 2. Raman spectrum of the multi-layered WS_2

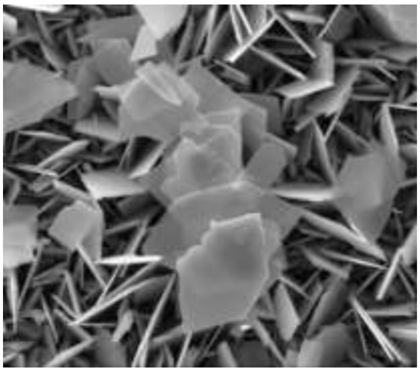

Fig. 3. ESEM image of MoS_2-MoO_2 film

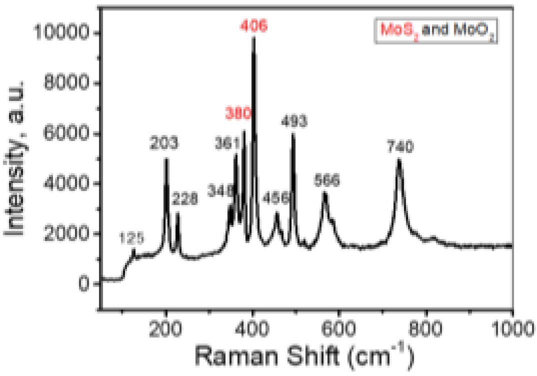

Fig. 4. Raman spectrum of MoS_2-MoO_2 film

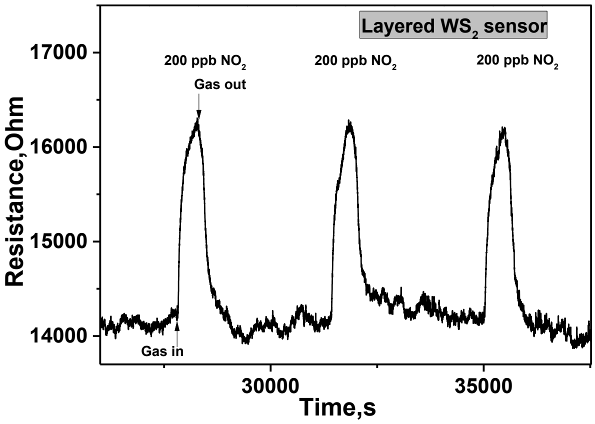

Fig. 5. WS_2 sensor response and recovery cycles towards 200 ppb of NO_2 at 250°C

3. Conclusion

2D films of layered WS_2 and MoS_2-MoO_2 were successfully deposited on silicon oxide substrate, using a hydrogen free, single step atmospheric pressure CVD approach. The obtained material (WS_2) was used as a resistive gas sensor. The results revealed that layered WS_2 led to the fabrication of a sensitive NO_2 sensor with a detection limit of 50 ppb. Work in this field will be continued, to improve further the sensitivity and detection limit of the sensor.

4. Acknowledgement

This project has received funding from the European Union's Horizon 2020 research and innovation programme under the Marie Skłodowska-Curie grant agreement No. 713679.

References

[1] C. Cong *et al.*, “Synthesis and optical properties of large-area single-crystalline 2D semiconductor WS2monolayer from chemical vapor deposition,” *Adv. Opt. Mater.*, vol. 2, no. 2, pp. 131–136, 2014.

Controlled fabrication of nanotubes from nanoporous anodic alumina

Jakub T. Domagalski, Elisabet Xifre-Perez, Josep Ferre-Borrull, Lluis F. Marsal*

Universitat Rovira I Virgili, Avinguda dels Països Catalans, 26, 43007 Tarragona, Spain.

* Lluis.marsal@urv.cat

Abstract

Herein, we report study leading to better understanding of pulse anodization AANTs manufacturing, increasing control over nanoparticle dimensions and properties employing both, different anodization conditions and post-fabrication treatment. Several AANTs characteristics like nanotube length, inner diameter, wall thickness, zeta potential and crystalline form were altered extending/expanding availability of this novel nanomaterial for future applications.

1. Introduction

Recent decades brought significant advances in the field of nanoporous materials. High surface area, well-defined pore size and functionalization possibilities are just a few of many features making nanoporous materials attractive in broad range of applications like catalysis, biomaterials and template to fabricate different nanostructured materials. Electrochemical anodization of aluminium is affordable and effective method to fabricate nanoporous structures made of anodic alumina (NAA). Tuning parameters of the process like voltage, current, electrolyte used and duration of the process, structures varying in shape and size can be synthesized [1]. Growing knowledge about effects of different parameters on characteristics of obtained structure led to design of more sophisticated fabrication methods, leading to creation of complex structures like nanopillars, funnels or rugate structures [1-3]. Another alternative may be to selectively split NAA into well-defined nanoparticles. This last approach is reported in this communication.

2. Materials and methods

Materials

Aluminium (Al) foils of thickness 0.5 mm and purity 99.999 % were supplied by Goodfellow Cambridge Ltd. Sulfuric acid (H_2SO_4) and ethanol (C_2H_5OH) were purchased from Scharlau. Cooper(II) chloride ($CuCl_2$), hydrochloric acid (HCl) and perchloric acid ($HClO_4$) were purchased from Sigma-Aldrich. Chemicals were used without further processing. PURELAB® Option-Q was chosen as source of ultrapure water for all the solutions used in this experiment.

Fabrication

Initially, Al discs 2cm in diameter were sonicated in ethanol and MiliQ water respectively, for 10 minutes each. Prior to anodization, Al discs were electropolished in mixture of $HClO_4$ and ethanol 1:4 (v:v) at 20 V and 5°C for 7 min. This was followed by the first anodization step in 0.3 M H_2SO_4 + 20% ethanol electrolyte at 25 V and 6°C for 20 h at potentiostatic conditions, providing MA-NAA layer of approximately 110 μm. Fig. 1 presents ESEM image of the bottom of MA-NAA organized array, just before applying pulse anodization.

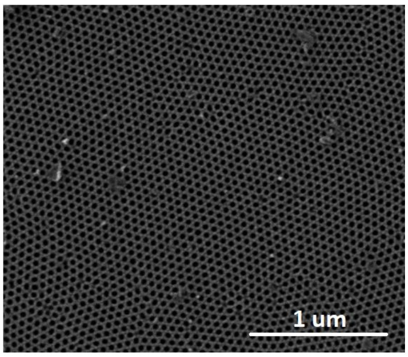

Fig. 1. ESEM image of MA-NAA backside.

Next, galvanostatic pulse anodization in 0.3 M H_2SO_4 modified with 10% ethanol at 1°C under vigorous stirring was carried out. PA was performed interlacing periods of different current density processes: mild anodization (4.5 mA/cm^2) for 5s and hard anodization (290 – 390 mA/cm^2) with duration between 2 and 3.5 s. Periodically altered PA-NAA morphology is shown on fig 2, thickness of each layer correspond to length of resultant AANTs. At last, remaining Al was removed by wet chemical etching in a mixture of 0.2 M $CuCl_2$ and 6.1 M HCl. After Al was removed, In order to additionally weaken connection between individual layers and cell junctions, sample was employed for additional 1 h of etching.

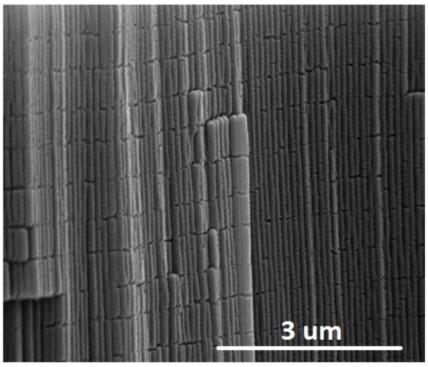

Fig. 2. ESEM image of PA-altered NAA.

NAA film was then subjected to mild sonication with different duration and at different temperatures. Fig. 3. shows nanotubes liberated after 1h sonication at ambient temperature.

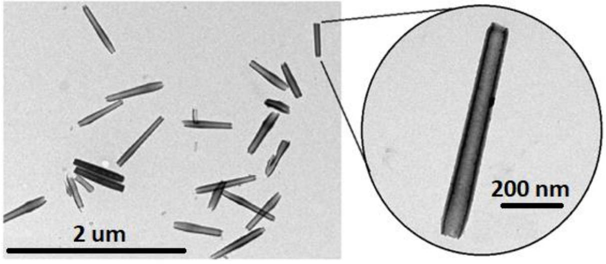

Fig. 3. TEM image of liberated AANTs

3. Results

Current density

To examine effects of current density during hard anodization on obtained structure, three different current densities have been applied during 2s hard anodization pulse: 292, 325 and 390 mA/cm^2, keeping other parameters unaltered. Fig. 4 gathers current/voltage profile of pulse anodization performed with different current density during HA.

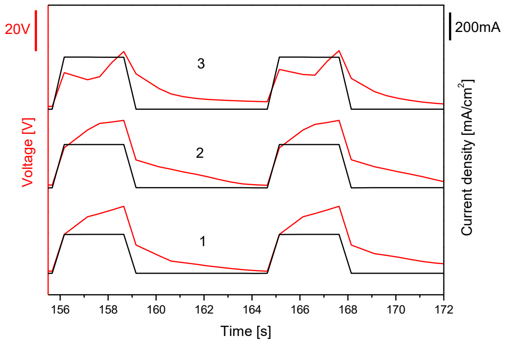

Fig 4. Current/voltage profiles of PA at different current density during HA. From left: 290, 325 and 390 mA/cm^2 respectively

Besides different length, inner diameter and wall thickness are affected as well. It is evident, that walls of nanotubes crafted during lower density pulses is thicker and walls are gradually thinner along with higher current values. Images of nanotubes fabricated applying different current have been gathered on fig. 5.

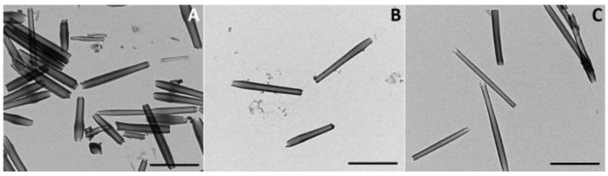

Fig 5. TEM images of AANTs fabricated at different HA current density.A, B, C corresponds to: 290, 325 and 390 mA/cm^2 respectively

Sonication temperature

Sonication temperature is important factor that can affect AANTs liberation efficiency. While it is generally expected, that lower temperatures result in higher efficiency to break unsoluble nanoparticles, different temperature may promote different breaking behaviour, thus different properties. TEM of AANTs treated with sonication at different temperatures is shown on fig. 6.

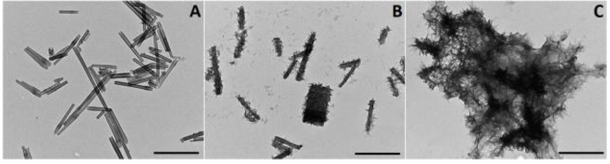

Fig 6. AANTS sonicated at different temperatures: A, B and C correspond to sonication temperature: 15, 40 and 65°C respectively. Scale bar: 1µm

It turns out, that sonication at temperatures above 30°C leads to fact collapse of occurring structure and fragmentation into nano-dust. Effect is more pronounced at higher temperatures.

4. Conclusions

Control over parameters of pulse anodization is important factor in design of resulting AANTs morphology and surface properties. While pulse duration provide convenient tool for simple length tailoring, current density changes allows to alter other AANTs properties as well. Not only it alter lenth of the tube, but can also be applied to alter wall thickness, inner diameter of the tube or zeta potential.

Acknowledgements

This work was supported in part by the Spanish Ministry of Economy and Competiveness TEC2015-71324-R (MINECO/FEDER), the Catalan authority AGAUR 2017-SGR-1527, and ICREA under the ICREA Academia Award. This project has received funding from the European Union's Horizon 2020 research and innovation programme under the Marie Sklodowska-Curie grant agreement No. 713679 and from the Universitat Rovira I Virgili (URV).

References

[1] T. Kumeria, A. Santos, M. M. Rahman, J. Ferre-Borrull, L. F. Marsal, D. Losic, ACS Photonics 1 (2014), 1298-1306.

[2] A. Santos, P. Formentin, J. Pallares, J. Ferre-Borrull, L. F. Marsal, Journal of electroanalytical chemistry, 655 (2011), 73-78.

[3] M. M. Rahman, E. Garcia-Caurel, A. Santos, L. F. Marsal, J. Pallares, J. Ferre-Borrull, Nanoscale research letters 7 (2012), 474-480.

Surface modification of Nanoporous Alumina towards bio-sensing applications in optical nano-fluidic system

L. Pol, L.K. Acosta, J. Ferré-Borrull, L.F. Marsal

Departament d'Enginyeria Electrònica, Elèctrica i Automàtica, Universitat Rovira i Virgili, Països Catalans 26, 43007, Tarragona, Spain
Lluis.marsal@urv.cat

Abstract

The chemical modification or functionalization of the surfaces of nanomaterials is a key step to achieve biosensors with the best sensitivity and selectivity.

In this work we propose nanoporous anodic alumina (NAA) functionalized with the streptavidin-biotin complex as a platform towards label-free biosensors. By means of reflective interferometric spectroscopy (RIfS), the streptavidin-biotinylated thrombin complex formation was monitored in real time. The study has permitted to establish the optimal streptavidin concentration that enables the efficient detection of the biotinylated thrombin. Finally, the ability of the NAA-RIfS system to quantify the concentration of biotinylated thrombin has been evaluated.

1. Introduction

Nanoporous anodic alumina is a material with growing interest in nanotechnology since it consists on an array of ordered straight pores perpendicular to the material surface obtained by the electrochemical anodization of aluminum in the appropriate conditions [1,2]. Thanks to its high surface-to-volume ratio, tailorable geometry and chemical stability NAA is widely used as a biosensing platform [3]. For this propose the surface modification of NAA by grafting functional molecules is a key step. The streptavidin-biotin interaction system is widely used in biosensors [4]. Thanks to their strong affinity and specificity, it is easy to immobilize any biotinylated molecule on a biosensor surface previously functionalized with and provide sensitivity for a great variety of analytes.

Optical biosensing with NAA has been demonstrated with the Reflection Interference Spectroscopy method [5]: the atachment of a specific chemical or biological molecule to the inner pore surface (conveniently modified) of a NAA thin film is detected by a change in the reflectance spectrum, quantified as a shift in the film effective optical thickness (EOT). In this work, we study the successive attachment of streptavidin and biotinylated thrombin to the inner pore NAA surface by means of RIfS. Furthermore, we study the capability of RIfS to detect different concentrations of biotinylated thrombin.

2. Experimental

NAA thin films were obtained following the two-step anodization process [1,2] using a 0.3 M oxalic acid electrolyte at an anodization potential of 40 V and at 4ºC in both anodization steps. Anodization time of the second step was adjusted to obtain a pore length of 5 µm. NAA were then immersed in 5% w/w H_3PO_4 for 20 min to adjust the pore diameter to 60 nm. Finally, 5 nm thickness gold film was deposited by sputtering on top of the NAA to increase contrast in the measured spectra.

Functionalization of the NAA started by immersing for 1h in boiling hydroxyperoxide (H_2O_2) with continuous stirring to obtain hydroxyl (-OH) groups on the surface. Next, hydroxylated NAA were incubated for 1h in 20 µl of dry toluene and with 0.2 µl of APTES added dropwise (under nitrogen flux), then NAA foils were rinsing with toluene and ethanol and storage overnight at 110 ^{0}C.

APTES-NAA samples were placed in the flow cell system to monitor the biotinylated thrombin attachment in NAA in real-time. Before each experiment, it was flowing PBS until a steady value of EOT registered. Simultaneously to this preparation step, streptavidin was incubated for 20 min with EDC and NHS in a proportion of 1:10:25, respectively, to activate the carboxyl groups of streptavidin.

The first step in the experiment was the injection of this activated streptavidin solution in the flow cell. In this first step, the free amino group of APTES (–NH3) formed a peptide bond with the carboxyl group of streptavidin (–COOH). This first step was applied until a stable EOT value was observed. After that, PBS was flowed to remove any non-specifically attached streptavidin molecules and finally different concentrations of biotinylated thrombin were flowed.

2. Results

It was studied the influence of the streptavidin concentration in the first step, Figure 5 shows the results of such study, where graphs a) to e) plot the change in EOT for the streptavidin binding step at concentrations of 50 µg/ml, 5 µg/ml, 3 µg/ml, 1 µg/ml and 0.5 µg/ml respectively. It was observed that the flow of the streptavidin solution resulted in a clear increase in EOT for all studied concentrations. The graphs a) to e) can be classified in two main groups: for the 50, 5 and 3 µg/ml concentrations two different stages in the EOT variation can be identified: a first one in which a fast increase in EOT is observed until it stabilizes in a short time (60 s for 50 µg/ml, 157 s for 5 µg/ml and 408 s for 3 µg/ml), followed by an inflexion point and a second stage with a slower increase rate. This second stage reaches a steady EOT value after a given time, at which PBS is introduced in the flow cell to remove all the non-bound molecules. However, for the 1 µg/ml and 0.5 µg/ml concentrations, only one stage is recognized: a fast increase in EOT that reaches a stable value in a short time and that is not followed by the second increase.

Furthermore, it was studied the influence of the biotinylated thrombin concentration, Figure 6a shows an example of the entire experiment where in the final step it was flowed 20 µg/ml biotinylated thrombin, it was observed that when biotinylated thrombin was flowed, an increase in EOT was observed and a stable EOT value is reached, and the level of EOT remains the same after the final wash step with PBS.

Figure 6 c) Shows a plot of the ΔEOT with respect to the biotinylated thrombin concentration. Experiments were performed for the 10, 20, 50, and 100 µg/ml concentrations in triplicates for each concentration. The reported value corresponds to the average of the three replicas, while error bars correspond to maximum and minimum measured ΔEOT. The graph indicates that thrombin can be clearly detected for concentrations above 10 µg/ml and that EOT response begins to saturate above 100 µg/ml.

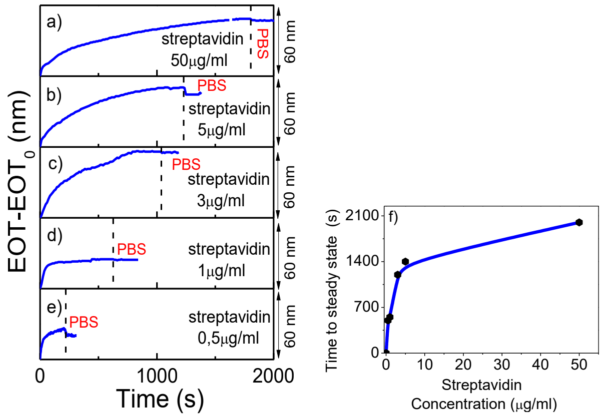

Figure1: Variation of EOT against time for the streptavidin attachment step for different streptavidin concentrations, indicated in the plots. a) 50 µg/ml, b) 5 µg/ml c) 3 µg/ml, d) 1 µg/ml and e) 0.5 µg/ml. f) Time to reach the steady state against streptavidin concentration.

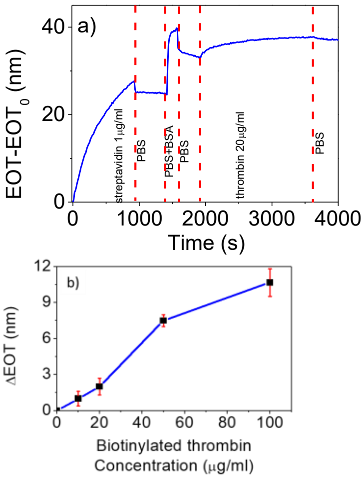

Figure 6: a) Example of EOT variation with time for a biotinylated thrombin attachment experiment intended to evaluate the sensitivity of the NAA platform, corresponding to the concentrations specified on the graph. b) Total change in EOT in the biotinylated thrombin attachment step (ΔEOT) against biotinylated thrombin concentration.

7. Conclusions

The capability NAA-based sensing of streptavidin-biotin attachment with RIfS has been demonstrated. Attachment of streptavidin, previously activated with EDC/HNS cross-linker, to the APTES is clearly shown in the RIfS experiments as an EOT increase. Furthermore, it was observed that the optimal concentration of streptavidin is 1 µg/ml.

We prove that this system is able to detect different concentrations of biotinylated thrombin. We prove that we are able to quantify the concentration of biotinylated molecules with a limit of detection of 4.47 µg/ml..

ACKNOWLEDGMENT

This study was supported by the Spanish Ministerio de Ciencia,Innovación y Universidades (MICINN/FEDER) RTI2018-094040-B-I00, by the Agency for Management of University and Research Grants (AGAUR) ref. 2017-SGR-1527 and by the Catalan Institution for Research and Advanced Studies (ICREA) under the ICREA Academia Award.

References

[1] Masuda; Fukuda, K. *Science*, **1995**, 268, 8–10.
[2] Santos, A. et. al., *Electroanal. Chem.* **2011**, 655, 73–78.
[3] T. Kumeria, et. al., *Biosensors and Bioelectronics*, **2012**, 35, 167–173
[4] J. H. Park, L. Gu, G. von Maltzahn, E. Ruoslahti, S. N. Bhatia, M. J. Sailor, *Nat. Mater.* **2009**, *8*, 331 – 336.
[5] Ferré-Borrull, et. Al. *Springer-Verlag Berlin*, **2015**, 185 – 217

Synthesis of new *n*-type molecules as Hole Transporting Materials for Perovskite Solar Cell

Dora González-Ruiz[a,b], Cristina Rodriguez-Seco[*,a] and Emilio Palomares[a,c,d]

[a]*Institute of Chemical Research of Catalonia (ICIQ), Avinguda del Països Catalans 16, 43007 Tarragona, Spain.*
Tel: +34 977 920 200; E-mail: dagonzalez@iciq.es
[b]*Universitat Rovira i Virgili (URV), N5- Edifici de Serveis Centrals Carrer Marcel·lí Domingo, 2-4-6, 43007- Tarragona*
[c]*Catalan Institution for Research and Advanced Studies (ICREA), Passeig de Lluis Companys 23, 08010 Barcelona, Spain.*
[d]*Universidad de Pau y Pays de l'Adour (UPPA), Avenue de l'Université, 64012 Pau, Francia*
Teléfono: +33 5 59 40 70 00.

Abstract

Nowadays, perovskite solar cells (PSCs) has attracted many attention due to its high efficiencies achieved and its low-cost fabrication procedures. 2,2′7,7′-tetrakis-(N,N-di-p-methoxyphenyl-amine)-9,9′-spirobifluorene (Spiro-OMeTAD) is the most used hole transporting material (HTM) for PSCs, reaching efficiencies up to 24.2 %[1]. However, its production cost, relative low hole mobility and difficult synthetic pathway with low yield are disadvantages that point out the need of designing and synthetizing new HTMs[2]. In this work, we report the synthesis of a carbazole-based novel HTM for PSCs (Figure 1).

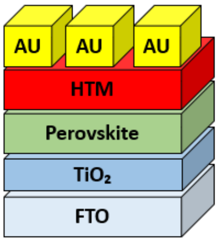

Figure 1: Schematic diagram of perovskite solar cell (PSC).

1. Introduction

Many attempts have been done in order to improve on the efficiency and stability of PSCs using other HTMs rather than Spiro-OMeTAD. HTMs based on the carbazole moiety (Scheme 1) have attracted attention due to their chemical structure has versatile and advantageous characteristics such as the low cost of the starting material (9H-carbazole), good chemical stability, easy functionalization and high solubility in common solvents among others[3].

2. HTM

The role of HTM in PSCs is extracting holes created in the perovskite when it absorbs light and transporting them towards the gold electrode (Au)[3]. For this reason, the principal characteristics that have to present a good HTM are: high hole mobility, good thermal and photochemical stability, energy levels (highest occupied molecular orbital, HOMO and the lowest unoccupied molecular orbital, LUMO) that fit with perovskite's, good photovoltaic parameters like large photocurrents, high open circuit voltage or fill factor and high solubility in common solvents[4].

Due to the optimal properties we mentioned before, a carbazole-based HTM was synthetized using a phenyl ring as core (CS06), shown in (Scheme 1).

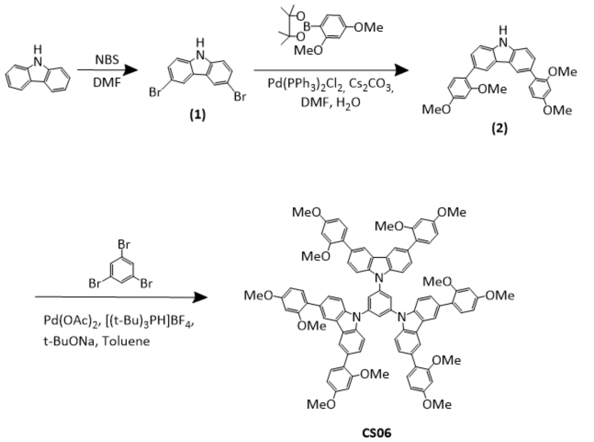

Scheme 1: Synthetic pathway for CS06.

3. Results and conclusions

The reactions involved in the synthesis of CS06 consisted first in a bromination with N-Bromosuccinimide (NBS) in DMF (1). After that, the coupling of the 1,3,-dimethoxybenzene units using Suzuki-coupling procedure (2). Finally, Buchwald-Hartwig amination was carried out using $Pd(OAc)_2$ as a catalyst to obtain the desired product CS06. Figure 2 show the ^1H NMR of CS06 data were in good agreement with the formula we report.

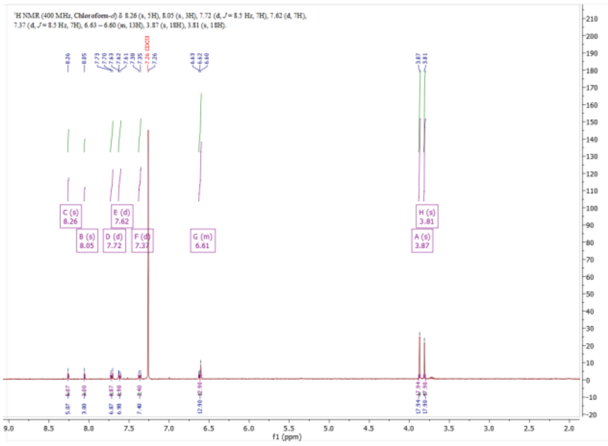

Figure 2. ^{1}H NMR (Chloroform-d) of CS06.

Before using CS06 as HTMs in PSCs, it is needed to do a full characterization doing ^{13}C-NMR, Mass Spectroscopy Absorption, Emission, cyclic voltammetry and other measurements like, TGA and DSC.

If the HOMO level is higher than the edge valence band of the perovskite and its LUMO level is high enough, we expect a similar or higher efficiency comparing with that of Spiro-OMeTAD.

4. References

[1] Kasparas Rakstys, Cansu Igci and Mohammad Khaja Nazeeruddin,"Efficiency vs. stability: dopant-free hole transporting materials towards stabilized perovskite solar cells", Chem. Sci., 2019, Advance Article.

[2] Ze Yu, Licheng Sun, "Recent Porgress on Hole-Transporting Materials for Emerging Organometal halide Perovskite Solar Cells", Adv. Energy Mater., 2015, 1500213.

[3] Sang Do Sung, Wan In Lee, "14.8% perovskite solar cells employing carbazole derivatives as hole transporting materials", Chem. Commun., 2014, 50, 14161-14163.

[4] Agarwala P, Kabra. "A review on triphenylamine (TPA) based organic hole transport materials (HTMs) for dye sensitized solar cells (DSSCs) and perovskite solar cells (PSCs): evolution and molecular engineering" J. Mater. Chem. A, 2017,5, 1348-1373.

[5] Adv. Mater. 2008, 20, 1357-1362.

[6] J. Mater. Chem. A, 2016,4, 15788-15822

Developing an Optimized Mass Spectral Library Search Algorithm for Compound Identification

J.M. Badia[1,2] , J. Capellades[1], O. Yanes[1], M. Vinaixa[1]

[1] MIL@b, Department of Electronic Engineering, Metabolomics Platform, IISPV, Universitat Rovira i Virgili
[2] Email: josepmaria.badia@estudiants.urv.cat

Abstract

We describe an optimized and computationally efficient mass spectral search algorithm for compound identification in liquid chromatography coupled to mass spectrometry (LC/MS)-based metabolomics. This algorithm is implemented in R and it is based upon cosine spectral similarity. It has been benchmarked against a test set of unknown tandem spectra (MS/MS) randomly selected from an in-house MS/MS library merged from publicly-available spectral repositories such as HMDB and MoNA

Introduction

Metabolomics is aimed at comprehensive study of cellular metabolism through simultaneously profiling as many metabolites as possible in a biological specimen [1]. Metabolite identification is a key mandatory step to obtain biologically interpretable results from this profiling. However, it remains the biggest bottleneck, particularly for untargeted metabolomics based on LC/MS [2,3]. High resolution mass spectrometry enables obtaining accurate molecular masses (MS1) from measured ions. Elemental composition, i.e., molecular formula can be inferred from accurate mass providing this way the most basic level of metabolite identification. However, this experimentally obtained molecular masses are not without an error. This error inflates the number of molecular formulas that can be reconstructed from a particular measured ion. Therefore a considerable number of metabolites cannot be resolved with the mass accuracy of current mass analyzers used in metabolomics. To this is added, the number of existing isobaric metabolites. Altogether this makes accurate mass measurements alone insufficient for metabolite identification. This accurate mass measurement should be ideally accompanied by MS/MS data which provides essential structural information to increase confidence in putative metabolite identification. Traditional LC-MS-based untargeted metabolomics workflow heavily relies on MS/MS spectra acquired either separately for those peaks of interest identified from previous MS1 runs or within the same run using data dependent acquisition modes (DDA). Putative identification is achieved in both cases by reconstructing the molecular formula from the precursor ion (MS1) and comparing its MS/MS spectra to those of model compounds in spectral repositories [4]. Thus, MS/MS spectral matching is intrinsically constrained to the particular subset of the whole spectral library with coincident molecular formulas with the precursor ion. However, the irruption of other MS/MS spectra acquisition modes such as data independent acquisition (DIA) [5] where no information is retained about the precursor ion, causes the necessity of a new conceptual matching algorithm where the spectra must be compared against the whole spectra library causing a considerable computational overload. The aim of this work is to develop a computationally efficient algorithm for spectral matching with minimum dependencies of constraining variables.

Methods

Algorithm programming and data analysis was conducted in R language using 3.6.0v version [6]

Results

An in-house MS/MS spectral repository

A local MS/MS spectral library named MS2ID was populated using both in-silico and experimentally obtained MS/MS spectra from publicly-available spectral repositories in HMDB [7] and MoNA (http://mona.fiehnlab.ucdavis.edu). The spectral data was downloaded as .xml and .json formats respectively and needed to be split into smaller files using a r5.xlarge Amazon instance (4CPU, 32GB RAM, 64-bit) due to the elevated RAM requirements. Data was parsed and manually curated to avoid redundancies. Spectra with the same fragmentation pattern and metabolites with identical inchikey were eliminated. Curated spectral data was merged in an R dataframe serving as an in-house optimized MS/MS spectral repository. Figure 1 shows the reduction ratios finally obtained in the number of spectra and metabolites, 75% and 80% respectively.

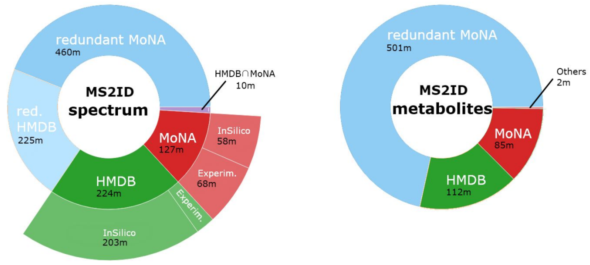

Fig.1. MS2ID composition and redundant data

Identification algorithm

We developed an optimized algorithm for unknown MS/MS spectra identification using MS2ID library. To this end we randomly selected 1000 MS2ID entries as representative MS/MS spectra test set. Spectra in this test set were noise-filtered by removing intensities below 1% of their maximum and binned to 0.01 Da. Subsequently, a cosine similarity was calculated between each individual pre-treated spectra in the test set and all those entries en MS2ID library sharing at least one common ion with the unknown spectra. As expected, we correctly identified all 1000 unknown spectra in the test set with a cosine similarity of 1. Figure 2 represents spectrum for the top scored spectra id=33384 together with their second best match.

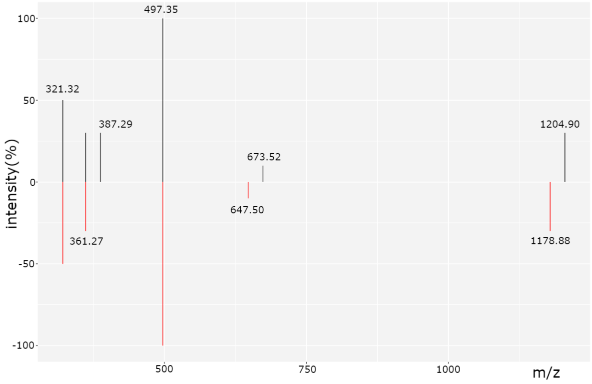

Fig.2. Unknown spectrum idespectra=33384 and its second best match, idespectra=66251, in red.

Identification algorithm computational performance

In order to demonstrate the performance of the identification algorithm, 200 identifications were made using randomly chosen unknown spectra with 10 or 30 masses resulting in a 1.9 s and 4.6 s mean operation time per spectrum respectively. A 64-bit Intel® Core™ i5-6600 CPU @ 3.30GHz × 4, 16 GiB was used, with no parallelization, under Ubuntu 18.04.2 LTS, R 3.6.0v and RStudio 1.2.1335v. Figure 3 shows how the number of fragments in the unknown spectrum affects the operation time.

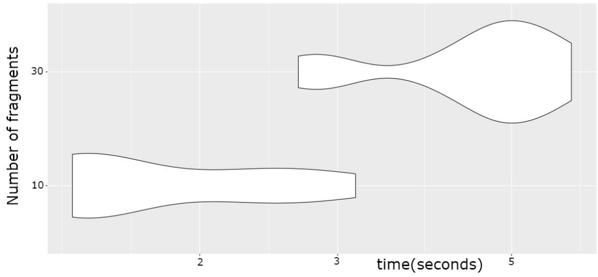

Fig.3. Density plot: identification running times of unknowns spectra containing 10 or 30 masses.

Future Work

We plan to expand the capabilities of our library search algorithm by including additional features on its scoring such as metadata regarding the occurrence of proposed candidates. On the other hand, we consider applying an ad-hoc binning based on the mass error spectra.

References

1. Newgard CB. Metabolomics and Metabolic Diseases: Where Do We Stand? Cell Metab. 2017;25: 43–56. doi:10.1016/j.cmet.2016.09.018

2. Niessen WMA. Liquid Chromatography | Mass Spectrometry☆. In: Worsfold P, Poole C, Townshend A, Miró M, editors. Encyclopedia of Analytical Science (Third Edition). Oxford: Academic Press; 2019. pp. 127–132. doi:10.1016/B978-0-12-409547-2.14213-1

3. Prasad B, Garg A, Takwani H, Singh S. Metabolite identification by liquid chromatography-mass spectrometry. Trends Analyt Chem. 2011;30: 360–387. doi:10.1016/j.trac.2010.10.014

4. Vinaixa M, Schymanski EL, Neumann S, Navarro M, Salek RM, Yanes O. Mass spectral databases for LC/MS- and GC/MS-based metabolomics: State of the

field and future prospects. Trends Analyt Chem. 2016;78: 23–35. doi:10.1016/j.trac.2015.09.005

5. Wang R, Yin Y, Zhu Z-J. Advancing untargeted metabolomics using data-independent acquisition mass spectrometry technology. Anal Bioanal Chem. 2019; doi:10.1007/s00216-019-01709-1

6. Team RC. R Core Team. A language and environment for statistical computing. R Foundation for Statistical Computing, Vienna, Austria 2015. ISBN 3--900051--07--0, URL http://www. R--project. org/. Available: http://www …; 2015.

7. Wishart DS, Feunang YD, Marcu A, Guo AC, Liang K, Vázquez-Fresno R, et al. HMDB 4.0: the human metabolome database for 2018. Nucleic Acids Res. 2018;46: D608–D617. doi:10.1093/nar/gkx1089

rMSIcleanup: an open-source computational tool for matrix-related peak annotation in MALDI-MSI

G. Baquer[1], P. Ràfols[1,2,3] , M. Garcia-Altares[1,2,3], LL. Sementé[1] , X. Correig[1,2,3]
[1]Department of Electronic Engineering, Rovira i Virgili University, Tarragona, Spain
[2]Spanish Biomedical Research Centre in Diabetes and Associated Metabolic Disorders (CIBERDEM), 28029, Madrid, Spain
[3]Institut d'Investigació Sanitària Pere Virgili, Tarragona, Spain

MALDI-MSI is a label-free technology that allows obtaining qualitative and quantitative molecular information together with spatial information from intact tissue sections. MALDI-MSI has been steadily adopted for spatially-resolved metabolomics and it has received much attention as a potential tool to understand mechanisms underlying complex diseases such as cancer or diabetes. However, conventional organic matrices used in MALDI cause spectral interferences in the low m/z range which seriously hamper metabolomics data processing.

Solutions to deal with data corruption due to matrix ion signals are nowadays tackled from two different perspectives. In one hand, the development of matrix-free approaches such as gold layer deposition (Au-LDI-MSI) [1] and on the other hand solutions based on post-processing computational tools [2].

Post-processing computational tools are easier to adapt by those laboratories without access to the specialized equipment required for matrix-free LDI-MSI. Several post-processing software solutions have successfully undertaken this issue relying on statistical heuristics or artificial neural networks [2]. Their holistic and unsupervised nature has proven suitable for automating the processing of large databases. However, meaningful information such as the molecular formula of the MALDI matrix is not exploited and they suffer from the black box problem as there is no clear way to trace back and justify the annotation.

We present rMSIcleanup, an open-source R package that relies on the chemical information of the matrix to annotate the matrix-related peaks. Given the matrix molecular formula, all possible theoretical adduct cluster patterns are calculated. For each cluster candidate, we compute cluster spectral similarity score (S1), intra-cluster morphological similarity score (S2) and mass tolerance similarity score (S3). Cluster peaks with high scores are considered present in the image and tagged as matrix-related. Additionally, as presented in Figure 1 the package uses a hierarchical clustering algorithm to detect and properly handle overlapping peaks allowing the processing of lower resolution datasets. The package offers a visual report that transparently justifies the annotation. The development version of rMSIcleanup is available at https://github.com/gbaquer/rMSIcleanup.

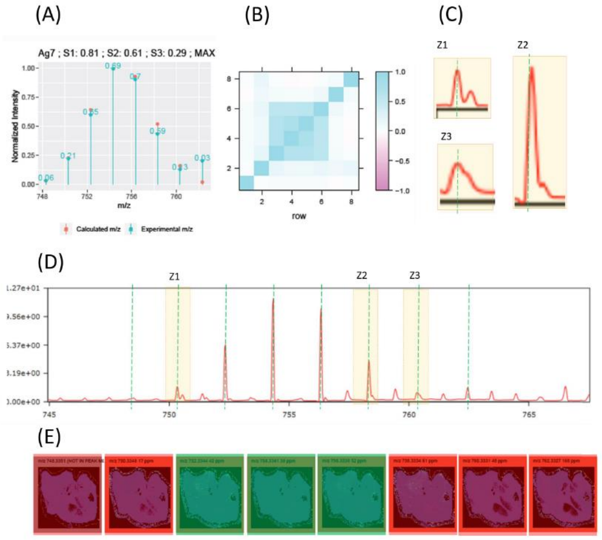

Fig.1. Initial similarity scores for an Ag7 cluster (positive class) are low due to overlapping peaks. Hierarchical clustering is used to detect overlapping peaks **A:** Experimental vs theoretical patterns. The peaks on the experimental peaks on the edges don't match the theoretical peaks. **B:** Correlation of the experimental images of the ions in the cluster. Peaks on the edges show a low correlation. **C:** Zoom-in regions of the mean spectrum with various degrees of overlapping **D:** Mean spectrum. **E:** Resulting classification of each ionic image after performing the overlapping detection. Green images are tagged as matrix-related without overlapping. Red images are tagged as matrix-related with overlapping.

As the first validation, rMSIcleanup was challenged using 14 images acquired with a sputtered silver nanolayer. Silver clusters previously reported in literature were consistently identified. On the other hand, chemically unfeasible cluster patterns showed lower similarity scores. Figure 2 shows the precision and recall curves for each of the proposed similarity metrics.

Additionally, a visual exploratory analysis was performed in all datasets to assess the impact of proper annotation and removal of the matrix-related peaks. Figure 3 depicts the spatial distribution of the first principal components when performing PCA before and after removing the matrix-related peaks. The removal of matrix-related peaks enhances contrast.

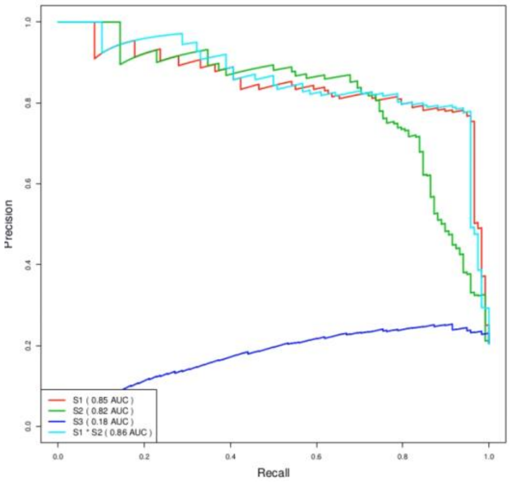

Fig.2. Precision and recall (PR) curve. The best performing score is the spectral similarity Score with an AUC of 0.838 followed by the morphological score S2 with an AUC of 0.793. The mass error tolerance score has proven not to be a useful indicator as it gives an AUC of 0.179.

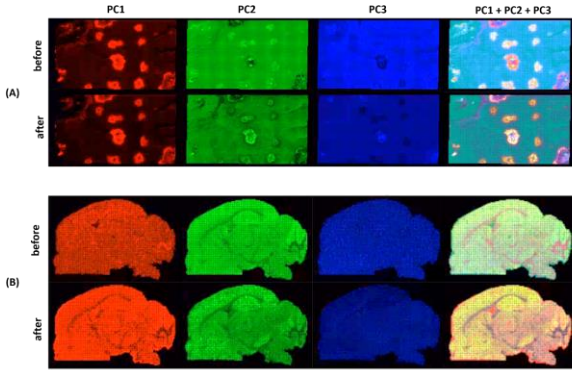

Fig. 3. Exploratory analysis with PCA before and after removing matrix-related peaks. The removal of the matrix leads to a generalized improvement of the contrast of morphological structures in all principal components. (A) Pancreas tissue. (B) Brain tissue.

A second validation step is in progress aiming to replicate the results using the most common MALDI-MSI images. This includes a dataset containing images acquired using the most common MALDI matrices and both TOF and FTICR spectrometers.

In conclusion, we have developed an open-source software tool that confidently annotates silver-related peaks in Ag-LDI-MS which anticipates its applicability to MALDI-MSI. Once demonstrated its performance in MALDI-MSI rMSIcleanup will pave the path to the use of common organic matrices for metabolomics studies.

References

[1] P. Ràfols *et al.*, "Assessing the potential of sputtered gold nanolayers in mass spectrometry imaging for metabolomics applications," 2018.

[2] K. Ovchinnikova, V. Kovalev, L. Stuart, and T. Alexandrov, "Recognizing off-sample mass spectrometry images with machine and deep learning."